r.avaflow v1, an advanced open source computational framework for the propagation and interaction of two-phase mass flows

Martin Mergili[1,2], Jan-Thomas Fischer[3], Julia Krenn[1,4], and Shiva P. Pudasaini[5]

[1] Institute of Applied Geology, University of Natural Resources and Life Sciences (BOKU), Peter-Jordan-Straße 70, 1190 Vienna, Austria

[2] Geomorphological Systems and Risk Research, Department of Geography and Regional Research, University of Vienna, Universitätsstraße 7, 1190 Vienna, Austria

[3] Department of Natural Hazards, Austrian Research Centre for Forests (BFW), Rennweg 1, 6020 Innsbruck, Austria

[4] Group Roads, Provincial Government of Lower Austria, Landhausplatz 1/17, 3109 St. Pölten, Austria

[5] Department of Geophysics, University of Bonn, Meckenheimer Allee 176, 53115 Bonn, Germany

Correspondence to: M. Mergili (martin.mergili@boku.ac.at)

Abstract

r.avaflow represents an innovative open source computational tool for routing rapid mass flows, avalanches or process chains from a defined release area down an arbitrary topography to a deposition area. In contrast to most existing computational tools, r.avaflow (i) employs a two-phase, interacting solid and fluid mixture model (Pudasaini 2012); (ii) is suitable for modelling more or less complex process chains and interactions; (iii) explicitly considers both entrainment and stopping with deposition, i.e. the change of the basal topography; (iv) allows for the definition of multiple release masses and/or hydrographs; and (v) serves with built-in functionalities for validation, parameter optimization and sensitivity analysis. r.avaflow is freely available as a raster module of the GRASS GIS software, employing the programming languages Python and C along with the statistical software R. We exemplify the functionalities of r.avaflow by means of two sets of computational experiments: (1) generic process chains consisting in bulk mass and hydrograph release into a reservoir with entrainment of the dam and impact downstream; (2) the prehistoric Acheron rock avalanche, New Zealand. The simulation results are generally plausible for (1) and, after the optimization of two key parameters, reasonably in line with the corresponding observations for (2). However, we identify some potential to enhance the analytic and numerical concepts. Further, thorough parameter studies will be necessary in order to make r.avaflow fit for reliable forward simulations of possible future mass flow events.

Keywords: GIS raster analysis, mass flows, open source, process chains, two-phase flow model

1 Introduction

Rapid flows or avalanches of snow, debris, rock or ice, or processes, process chains or process interactions involving more than one type of movement or material frequently lead to loss of life, property and infrastructures in mountainous areas worldwide. All state-of-the-art methods for anticipating the occurrence, characteristics, and dynamics of such events rely on computer simulations. On the one hand, models attempt to identify those areas where mass flows are likely to release (landslide susceptibility; Guzzetti, 2006; Van Westen et al., 2006). On the other hand, they attempt to anticipate the motion of rapid mass flows once they are released (Hungr et al., 2005a). Whilst conceptual models (Lied and Bakkehøi, 1980; Gamma, 2000; Wichmann and Becht, 2003; Horton et al., 2013; Mergili et al., 2015) are employed to identify possible impact areas at broad scales, physically-based dynamic models are used for the detailed back-analysis or prediction of specific events.

Advanced fluid dynamics offers a broad array of physically-based dynamic modelling approaches for mass flows, mostly referred to as granular avalanches or debris flows. Such models often centre on two-dimensional "shallow flow" equations, but they vary considerably among themselves in terms of their concept, complexity and capacity to model specific types of phenomena. Voellmy (1955) pioneered mass flow modelling, followed by the work of Grigoriyan et al. (1967); Savage and Hutter (1989) ; Takahashi (1991); Iverson (1997); Pitman and Le (2005); and many others (see Pudasaini and Hutter, 2007 for a review). Savage and Hutter (1989) introduced depth-averaged mass and momentum conservation equations which were later utilized, modified and extended by Mangeney et al. (2003, 2005); Denlinger and Iverson (2004); and McDougall and Hungr (2004, 2005). The Savage and Hutter (1989) model was further extended to include the effects of pore fluid by Iverson and Denlinger (2001); Savage and Iverson (2003); Pitman and Le (2005); Pudasaini et al. (2005); Pastor et al. (2009); and Hutter and Schneider (2010a, b). Still, these approaches either represent effectively one-phase models, or do not fully consider the two-phase nature of most mass flows. More recently, the software GeoClaw and its extension D-Claw consider shallow water and quasi two-phase flows (Berger et al., 2011; Iverson and George, 2016). Pudasaini (2012) introduced a general two-phase mass flow model including several essentially new physical aspects of two-phase solid-fluid mixture flows. In comparison to one phase models, this amongst few other two-phase approaches (e.g. Kowalski and McElwaine, 2013) appears suitable for the realistic simulation of most types of process chains and interactions such as overtopping of a lake and a subsequent flood or debris flow due to the impact of a landslide into the lake.

Entrainment of the basal material into the flow may substantially alter the dynamics and characteristics of mass flows, increasing their destructive potential (Hungr and Evans, 2004; Hungr et al., 2005b; Reid et al., 2011; Berger et al., 2011; Pirulli and Pastor, 2012). Empirical laws for entrainment were proposed by Rickenmann et al. (2003); McDougall and Hungr (2005); and Chen et al. (2006), whereas mechanical concepts were introduced by Fraccarollo and Capart (2002); Pitman et al. (2003a); Sovilla et al. (2006); Medina et al. (2008); and Iverson (2012). The available entrainment models are effectively single-phase, and developed for bulk debris (Armanini et al., 2009; Crosta et al., 2009; Hungr and McDougall, 2009; Pirulli and Pastor, 2012). Whilst the im-

portance of erosion, and the associated change of the basal topography (Fraccarollo and Capart, 2002; Hungr and Evans, 2004; Hungr et al., 2005b; Le and Pitman, 2009) has been recognized by the scientific community, attempts to simulate deposition of mass flow material are sparsely documented.

Various types of numerical schemes have been used to solve mass flow model equations in order to redistribute mass and momentum (e.g. Davis, 1988; Toro, 1992; Nessyahu and Tadmor, 1990; Tai et al., 2002; Wang et al., 2004). Previously, equations were commonly formulated and solved for pre-defined types of topographies (Pudasaini et al., 2005, 2008; Wang et al., 2004) whereas a mathematically consistent application to arbitrary mountain topographies – and therefore to real-world conditions – still remains a challenge (Mergili et al., 2012). This issue is closely related to the fact that the model equations are commonly expressed in topography-following coordinates hardly compatible with global Cartesian coordinates, which usually appear in Geographic Information Systems (GIS) and are referred to as GIS coordinates in the following. Nevertheless, some of the mass flow models mentioned have been implemented in computational tools used for hazard mapping and zoning, such as DAN (Hungr et al., 1995); TITAN2D (Pitman et al., 2003b; Pitman and Le, 2005); SamosAT (Sampl and Zwinger, 2004); or RAMMS (Christen et al., 2010a, b). Hergarten and Robl (2015) developed a modelling tool relying on the open source flow solver GERRIS (Popinet, 2009).

None of these models explicitly consider stopping and deposition, and they offer only basic functionalities for simulating chains or interactions of two-phase mass flows. There is, however, a particular need to appropriately consider process chains and interactions in mass flow simulations: some of the most destructive events in history have evolved from cascading effects, such as the 1970 Huascarán event in Peru (Evans et al., 2009) or the 2002 Kolka-Karmadon event in Russia (Huggel et al., 2005).

The present work addresses some of the needs and issues raised by introducing the multi-functional open source computational framework r.avaflow, employing an enhanced version of the Pudasaini (2012) two-phase flow model for routing mass flows from a defined release area down arbitrary topography to a deposition area. Next, we introduce the structure and components of r.avaflow (Sect. 2). Then we perform two computational experiments in order to demonstrate the functionalities of the computational framework (Sect. 3). We discuss the implementation of r.avaflow and the implications of our findings (Sect. 4), and finally conclude with the key messages of the work and a brief outlook to the next steps (Sect. 5).

2 The computational framework r.avaflow

2.1 Computational implementation

r.avaflow computes the propagation of mass flows from one or more given release areas over a defined basal topography until (i) all the material has stopped and deposited; (ii) all the material has left the area of interest; or (iii) a user-defined maximum simulation time has been reached.

112 r.avaflow is developed along two lines with regard to its software environment and operation,
113 r.avaflow [EXPERT] and r.avaflow [PROFESSIONAL]. The latter represents a stand-alone version
114 with still reduced functionalities. It is operated through a graphical user interface (GUI), suitable
115 for practitioners. The present work, however, refers to r.avaflow [EXPERT] which is implemented
116 as a raster module of the open source software package GRASS GIS 7 (Neteler and Mitasova, 2007;
117 GRASS Development Team, 2016). We use the Python programming language for data manage-
118 ment, pre-processing and post-processing tasks (module r.avaflow). The flow propagation proce-
119 dure (see Sect. 2.3 and 2.4) is written in the C programming language (sub-module
120 r.avaflow.main). Together with Python, the R software environment for statistical computing and
121 graphics (R Core Team, 2016) is employed for built-in validation and visualization functions.
122 Fig. 1 illustrates the logical framework of r.avaflow.

123 Multiple model runs may be executed in parallel, exploiting all computational cores available (see
124 Sect. 2.5). This speeds up the processing considerably, and allows the use of r.avaflow on computa-
125 tional clusters. Parallelization is implemented at the Python level (Mergili et al., 2014, 2015): for
126 each model run a batch file is produced within the module r.avaflow. This batch file calls the Py-
127 thon-based sub-module r.avaflow.mult, launching r.avaflow.main which is then executed with the
128 specific parameters for the associated model run. Thereby, the Python library "Threading", a high-
129 er-level threading interface is exploited. The Python class "Queue" is employed for handling the
130 queue of items to be processed.

131
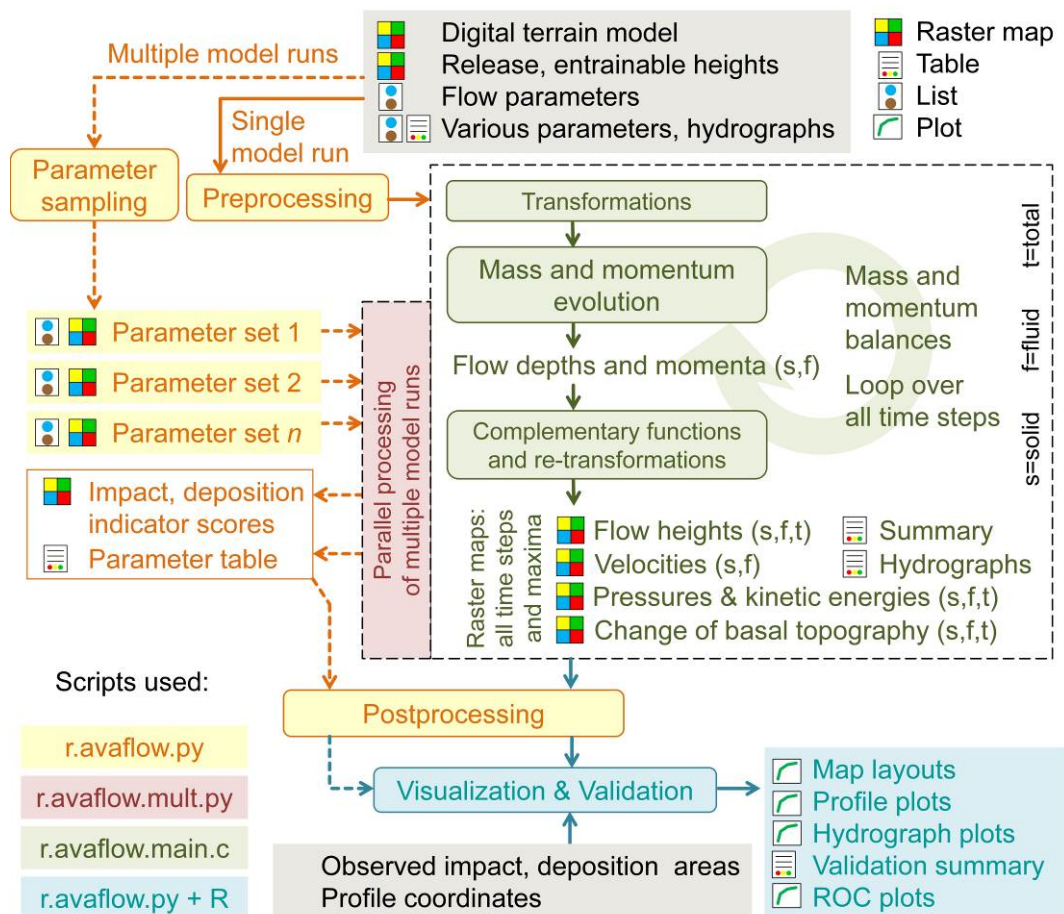
Figure 1 Logical framework of r.avaflow. The transformations and re-transformations refer to the conversion of heights and GIS coordinates to depths and topography-following coordinates, and vice versa (see Sect. 2.3).

r.avaflow was developed and tested with the operating systems (OS) Ubuntu 12.04 LTS and 16.04 LTS, and Scientific Linux 6.6 (Red Hat). It is expected to work on other UNIX systems, too. A simple user interface is available. However, the tool may be started more efficiently through command line parameters, enabling a straightforward batching on the shell script level. This feature facilitates model testing and the combination with other GRASS GIS modules.

Experiments where parallel processing is not applied are performed on an Intel® Core i7 975 with 3.33 GHz and 16 GB RAM (DDR3, PC3-1333 MHz), exploring a maximum of eight cores through hyperthreading and using the OS Ubuntu 12.04 LTS. All experiments with parallel processing are performed on the Vienna Scientific Cluster, serving with approx. 2020 nodes (Supermicro X9DRD-iF Board), each equipped with two Intel Xeon E5-2650v2 with 2.6 GHz und $8 \cdot 8$ GB RAM. The OS for these computations is Scientific Linux 6.6 (Red Hat).

2.2 Input and output

The key input parameters of r.avaflow are summarized in Table 1. Essentially, r.avaflow relies on (i) a digital terrain model (DTM) representing the elevation of the basal surface (in the release areas beneath the release mass) before the event under investigation; (ii) raster maps of the spatial distribution of the solid and fluid release heights or hydrographs of solid and fluid release; (iii) a set of flow parameters (Table 2). Input raster maps of the entrainable solid and fluid heights, and a raster map or value defining the empirical entrainment coefficient (needed for entrainment) are optional. Instead of the solid and fluid release and entrainable heights, the total heights and fixed values of the solid concentration may be defined.

There is no restriction imposed on the arrangement of the release cells. With the term 'cell' we refer to a regular, square, equidistant, ground projected computational/numerical unit, i.e. an element of a GIS raster. Patches of cells where the release height is larger than zero may be defined in various parts of the investigation area. An arbitrary number of release hydrographs – each associated to a given set of coordinates – can be defined alternatively or in addition to the different release masses. This allows the simulation of complex interactions between different types of processes (see Sect. 3). Hydrographs are defined through their solid and fluid heights at the centre point of the hydrograph profiles, and by the solid and fluid flow velocities. The flow height distribution along the hydrograph profile – which should be aligned perpendicular to the main flow direction – is derived from the assumptions of a horizontal cross section of the flow table and a maximum profile length (Fig. 2).

Central flow height H_P (solid + fluid) defined along with cross-profile velocities v_P (solid, fluid)

Basal topography

Input hydrographs: H_s / H, v = constant along profile

Profile width

Solid (s) discharge: $Q_s = \Sigma(H_{n,s} \cdot w) \cdot v_{P,s}$

Fluid (f) discharge: $Q_f = \Sigma(H_{n,f} \cdot w) \cdot v_{P,f}$
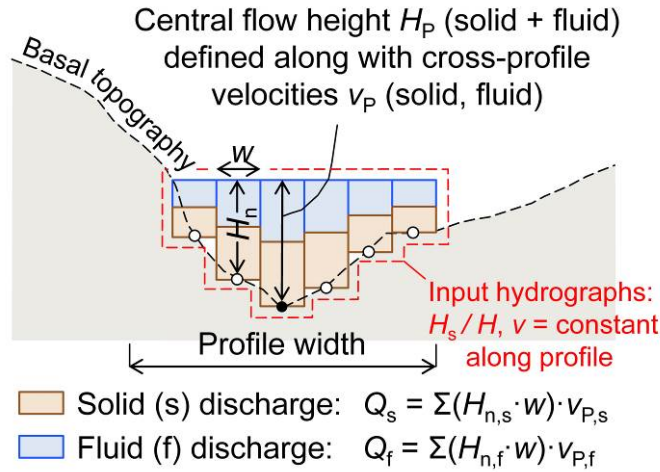
Figure 2 Sketch of a hydrograph profile. The flow surface of input hydrographs is defined by H_P and is extended in cross-profile direction either to the edge of the profile or until it intersects with the basal topography.

Table 1 Key input and output parameters of r.avaflow. s = solid; f = fluid; t = total. Remarks: 1 – mandatory; 2 – one of the input data sets A, B or C+D is mandatory, C+D may also be provided in addition to A or B; $n_D \geq n_C$, if $n_D > n_C$ the remaining sets of D are output hydrographs; 3 – either A or B may be provided if entrainment is activated, otherwise all values of $H_{Emax} = \infty$; C is mandatory with entrainment; 4 – at least one of the data sets A, B and C is mandatory for validation.

Parameter	Symbol	Unit	Format	Remarks
Input				
Initial elevation of basal surface	Z_0	m	Raster map	1
s, f release heights	$H_{0,s}$, $H_{0,f}$	m, m	Raster maps	2A
Total release height, s concentration of release mass	H_0, α_{s0}	m, −	Raster map, value	2B
s, f entrainable heights	$H_{Emax,s}$, $H_{Emax,f}$	m, m	Raster maps	3A
Entrainable total height, s concentration of entrainable mass	H_{Emax}, $\alpha_{s,Emax}$	m, −	Raster map, value	3B
n_C hydrograph tables: s and f flow heights and velocities at defined points of time (see Fig. 2)	$H_{P,s}$, $v_{P,s}$ $H_{P,f}$, $v_{P,f}$	m, m s^{-1} m, m s^{-1}	Tables	2C
n_D sets of centre coordinates, length and aspect of hydrograph	−	m, degree	Sets of four values	2D
Flow parameters (see Table 2)	−	−	Set of 14 values	1
Entrainment coefficient (see Table 2)	C_E	kg^{-1}	Value	3C
Time interval for output, max. time after which simulation terminates	Δt_{out}, t_{term}	s, s	Set of 2 values	1
Threshold flow height for visualization and validation	H_t	m	Value	1
Observed impact area, observed deposition area	OIA, ODA	−, −	Raster maps	4A, B
Vertex coordinates of flow path	−	m	Even number of ≥4 values	4C

Output (excluding validation and visualization output; see Sect. 2.6)				
Maximum flow height, kinetic energy, and pressure (each for s, f, t)	H_{Max}, T_{Max}, p_{Max}	m, J, Pa	Raster maps	Always
Flow height, flow kinetic energy, and flow pressure at each output time step t_{out} (each for s, f, t)	H_{tout}, T_{tout}, p_{tout}	m, J, Pa	Raster maps	Always
Flow velocities in x and y direction, and in absolute values (each for s, f)	v_x, v_y, v	m s^{-1}	Raster maps	Always
Change of basal topography (s, f, t)	H_C	m	Raster maps	Always
Impact indicator index, deposition indicator index	III, DII	–, –	Raster maps	Multiple runs
n_D-n_C output hydrograph tables: flow heights, velocities and discharges at defined points of time (s, f)	H_P, v_P, Q	m, m s^{-1}, m^3 s^{-1}	Tables	If $n_D > n_C$

176 Mandatory parameters further include the time interval at which output maps are written Δt_{out} (s),
177 the maximum time after which the simulation terminates, and the threshold flow height for visu-
178 alization and validation H_t (m; see Table 1). Optional parameters further include raster maps of the
179 observed impact area and deposition height as well as a set of flow path coordinates (for validation
180 and visualization; see Fig. 1 and Sect. 2.6). An exhaustive list of input parameters is provided in the
181 user manual of r.avaflow, available at http://www.avaflow.org/software.html.

182 If a single model run is executed (see Fig. 1), the output of r.avaflow consists in raster maps of sol-
183 id, fluid and total flow heights, flow velocities in x and y direction and in absolute terms, pressures
184 and kinetic energies, and the change of the basal topography (only relevant with entrainment or
185 stopping; see Sect. 2.4). All raster maps are produced for each output time step (defined by Δt_{out})
186 and for the maximum over all time steps. Further, a table summarizing the maximum solid and
187 fluid flow heights and velocities as well as flow volumes and kinetic energies for all output time
188 steps is produced. Optionally, solid and fluid output hydrographs are generated for an arbitrary
189 number of given output hydrograph profiles (see Table 1 and Fig. 2). With multiple model runs,
190 the results of each single run are aggregated to impact or deposition indicator indices (see
191 Sect. 2.5). In the present work we focus on the output heights, hydrographs and indices when ana-
192 lyzing the results, rather than on velocities or deduced results such as pressures or kinetic energies
193 (see Sect. 3).

2.3 Mass and momentum evolution

195 The core functionality of r.avaflow consists in the redistribution of mass and momentum, employ-
196 ing a dynamic flow model and a numerical scheme. Thereby the tool offers implementations (i) of
197 a single-phase shallow water model with Voellmy friction relation (Christen et al., 2010a, b;
198 Fischer et al., 2012) and (ii) essentially the Pudasaini (2012) two-phase flow model with ambient
199 drag (Kattel et al., 2016) and a set of additional numerical treatments (complementary functions)
200 outlined in Sect. 2.4. In the present work we only consider the implementation (ii). It builds on
201 the conservation of mass and momentum, computed separately but simultaneously for the solid

202 and fluid components of the flow. A system of six differential equations (expressed in locally to-
203 pography-following coordinates) represents the basis for a set of six flux and source terms, regard-
204 ing solid and fluid flow depths (D_s, D_f), solid momentum M_s and fluid momentum M_f in x direction
205 ($M_{sx} = D_s \cdot v_{sx}$, $M_{fx} = D_f \cdot v_{fx}$), and M_s and M_f in y direction ($M_{sy} = D_s \cdot v_{sy}$, $M_{fy} = D_f \cdot v_{fy}$), where v is
206 flow velocity.

207 The Pudasaini (2012) model employs the Mohr-Coulomb plasticity for the solid stress. The fluid
208 stress is modelled as a solid-volume-fraction-gradient-enhanced non-Newtonian viscous stress.
209 The generalized interfacial momentum transfer includes viscous drag, buoyancy, and virtual mass
210 induced by relative acceleration between the phases. A new, generalized drag force is proposed
211 that covers both solid-like and fluid-like contributions. Strong coupling between the solid- and
212 the fluid-momentum transfer leads to simultaneous deformation, mixing, and separation of the
213 phases. Inclusion of the non-Newtonian viscous stresses is important in several aspects. The advec-
214 tion and diffusion of the solid volume fraction play an important role. The model includes a num-
215 ber of innovative, fundamentally new, and dominant physical aspects. Please consult Pudasaini
216 (2012) for the full details of the model, including the corresponding equations. The flow parame-
217 ters required are summarized in Table 2.

218 Solving the differential equations and propagating the flow from one cell to the next requires the
219 implementation of a numerical scheme. For this purpose r.avaflow employs a high resolution Total
220 Variation Diminishing Non-Oscillatory Central Differencing (TVD-NOC) Scheme, a numerical
221 scheme useful to avoid unphysical numerical oscillations (Nessyahu and Tadmor, 1990). Cell aver-
222 ages of all six state variables are computed using a staggered grid: the system is moved half of the
223 cell size with every time step, the values at the corners of the cells and in the middle of the cells
224 are computed alternatively at half and full time steps, respectively. The TVD-NOC scheme with
225 the Minmod limiter has successfully been applied to a large number of mass flow problems (Tai et
226 al., 2002; Wang et al., 2004; Mergili et al., 2012; Pudasaini and Krautblatter, 2014; Kafle et al.,
227 2016; Kattel et al., 2016).

228 Table 2 Flow parameters and entrainment coefficient required with the enhanced version of the
229 Pudasaini (2012) two-phase flow model. Exp. 1 and 2 refer to the values used for the computation-
230 al experiments introduced in Sect. 3.

Symbol	Parameter	Unit	Exp. 1A, B, C	Exp. 2A, B
ρ_s	Solid material density (grain density)	kg m^{-3}	2700	2700
ρ_F	Fluid material density	kg m^{-3}	1000	1000
φ	Internal friction angle	Degree	35	35
δ	Basal friction angle [1]	Degree	20	15–25, 17
C_{VM}	Virtual mass	–	0.5	0.5
v_T	Terminal velocity	m s^{-1}	1	1
P	Parameter for combination of solid- and fluid-like contributions to drag resistance	–	0.5	0.5
Re_P	Particle Reynolds number	–	1	1
J	Exponent for drag (1 = linear, 2 = quadratic)	–	1	1
N_R	Quasi Reynolds number	–	30,000	30,000

N_{RA}	Mobility number	–	1,000	1,000
χ	Viscous shearing coefficient for fluid	–	0	0
ξ	Solid concentration distribution with depth	–	0	0
C_{AD}	Ambient drag coefficient [2]	–	0	0
C_E	Entrainment coefficient [1]	kg^{-1}	–, $10^{-5.3}$, $10^{-6.0}$	–

[1] Alternatively, these parameters may be provided as raster maps instead of global values; [2] Refer to Kattel et al (2016) for ambient drag

The input and output of r.avaflow (see Sect. 2.2) is discretized on the basis of GIS coordinates, i.e. in cells which are rectangular in shape in the ground projection. For the numerical solution the cell lengths in x and y directions, and the area, are corrected for the local slope in order to maintain consistency with the state variables expressed in the local topography-following coordinates. Gravitational acceleration in the topography-following x, y, and z directions – representing a fundamental input to the Pudasaini (2012) model equations – is computed from the DTM, employing a finite central difference scheme. All input heights H (m) are expressed in vertical direction, and are converted into depths D (m) expressed in direction normal to the local topography as in the model equation formulation. The resulting depths are converted into heights for output. The time step length Δt is dynamically updated according to the CFL condition (Courant et al., 1967; Tai et al., 2002; Wang et al., 2004).

We note that all total (solid + fluid) heights and depths represent the real-world heights and depths only if all the pores in the solid material are filled with fluid (pores filled with air are excluded).

2.4 Complementary functions

Table 3 summarizes some additional functions of r.avaflow. The functions with ID 1–3 have been introduced to compensate for deficiencies of the numerical scheme and its implementation experienced with complex real-world flows (see Sect. 4). Entrainment and stopping, in contrast, represent dynamic functions not covered by the Pudasaini (2012) model and are executed at the end of each time step (see Fig. 1). Even though the separation of the complementary functions from the TVD-NOC scheme, and their treatment in a simple forward Euler manner, can be questioned physically and mathematically, we consider the current implementation a reasonable first approximation (see Sect. 4). We now elaborate the concepts employed for entrainment as well as for stopping and deposition in more detail.

Table 3 Functionalities of r.avaflow introduced for numerical purposes (ID 1–3) or complementing the Pudasaini (2012) model (ID 4,5). Exp. 1 and 2 refer to the computational experiments introduced in Sect. 3; Y = activated; N = deactivated.

ID	Function	Description	Exp. 1ABC	Exp. 2AB
1	Diffusion control	Propagation of the flow from one cell to the next is suppressed if the velocity is	YYY	YY

				YYY	YY
		not high enough, reducing numerical diffusion			
2	Conservation of volume	Flow volume lost due to numerical reasons is replaced through an increase of D of all cells by the fraction of lost volume after each time step		YYY	YY
3	Surface control	Numerical oscillations of undisturbed flat surfaces (such as reservoirs) are avoided		YYY	NN
4	Entrainment	Empirical approach to compute entrainment of basal material		NYY	NN
5	Stopping and deposition	Energy balance approach for stopping and deposition of flow material		NNN	YY

261

262   Full handling of the evolution of the basal topography within the TVD-NOC scheme is not
263   straightforward and could also produce some diffusion. Therefore, and as entrainment is not in-
264   cluded in the original Pudasaini (2012) model, entrainment is treated as a complementary function
265   in a first step. We note, however, that the time steps at which entrainment and the change of the
266   basal topography are updated are identical to the time steps of the numerical scheme. The poten-
267   tial solid and fluid entrainment rates $q_{E,s}$ and $q_{E,f}$ (expressed perpendicular to the basal topography)
268   build on the user-defined empirical entrainment coefficient C_E (see Table 2) and the solid and flu-
269   id momenta. We assume a vertically homogeneous solid fraction $\alpha_{s,Emax}$ within the entrainable ma-
270   terial, which is reflected in the ratio between $q_{E,s}$ and $q_{E,f}$:

271
$$q_{E,s} = C_E \left| M_s + M_f \right| \alpha_{s,Emax}, \quad q_{E,f} = C_E \left| M_s + M_f \right| \left(1 - \alpha_{s,Emax} \right). \tag{1}$$

272   The fact that the basal velocities, which are relevant for entrainment, are lower than the depth-
273   averaged velocities is not explicitly considered, but has to be reflected in the value of C_E. $q_{E,s}$ and
274   $q_{E,f}$ are always positive. The solid and fluid changes of the basal topography $H_{E,s}$ and $H_{E,f}$ due to en-
275   trainment are:

276
$$H_{E,s,t} = \min\left(H_{E,s(t-\Delta t)} + \frac{q_{E,s}\Delta t}{\cos\beta}, H_{Emax,s} \right), \tag{2}$$

277
$$H_{E,f,t} = \min\left(H_{E,f(t-\Delta t)} + \frac{q_{E,f}\Delta t}{\cos\beta}, H_{Emax,f} \right), \tag{3}$$

278   where $H_{E,s(t-\Delta t)}$ and $H_{E,f(t-\Delta t)}$ are the change of the basal topography at the start of the time step, $H_{Emax,s}$
279   and $H_{Emax,f}$ are the maximum entrainable depths at the given cell, t is the time passed at the
280   end of the time step, Δt is the time step length, and β is the local slope of the basal surface. The
281   division by $\cos\beta$ approximates the conversion from depths to heights. The solid and fluid en-
282   trained depths $D_{E,s} = (H_{Es,t} - H_{Es(t-\Delta t)}) \cos\beta$ and $D_{E,f} = (H_{Ef,t} - H_{Ef(t-\Delta t)}) \cos\beta$ are added to the solid and
283   fluid flow depths. We further assume that entrainment increases the solid and fluid momentum of
284   the flow in each direction by the product of the entrained solid and fluid depth and the velocity in
285   the given direction (M_E; Fig. 3a). The basal topography and, consequently, the x and y cell sizes,

286 cell areas, and gravitational acceleration components in x, y, and z direction are updated after each
287 time step.

288 The changes in gravitational acceleration also influence the magnitude of the frictional terms
289 (Pudasaini and Hutter, 2003), which are important for stopping processes. In the literature few
290 approaches explicitly consider stopping processes directly in their numerical scheme by operator
291 splitting methods coupled with the determination of admissible stresses (e.g. Mangeney et al.,
292 2003; Zhai et al., 2015). Here, in order to consider stopping which occurs at a spatial scale that is
293 not numerically resolved, we choose a different approach by proposing the dimensionless factor of
294 mobility *FoM*, relating the distance required for stopping s_{stop} to the numerical spatial resolution
295 Δs in the direction of movement. The flow stops if $s_{stop} \leq \Delta s$, i.e. $FoM \leq 1$ (see Fig. 3b):

$$FoM = \frac{s_{stop}}{\Delta s}. \tag{4}$$

297 To estimate s_{stop} we formulate the energy balance considering that the initial kinetic energy at an
298 initial velocity v_0 and the change of potential energy while travelling the distance s_{stop} have trans-
299 formed in dissipative energy due to Coulomb friction, which dominates close to stopping. With
300 this the energy balance estimate yields:

$$\frac{v_0^2}{2} + s_{stop} \sin \beta_v g = s_{stop} \tan \delta \cos \beta_v g. \tag{5}$$

302 Consequently,

$$s_{stop} = \frac{v_0^2}{2g \cos \beta_v (\tan \delta - \tan \beta_v)}, \tag{6}$$

304 where δ is the basal friction angle, β_v is the slope angle in the direction of movement, and g is
305 gravitational acceleration (see Table 2). According to Eq. 6 the stopping distance s_{stop} is positive for
306 $\delta > \beta_v$, meaning that stopping is possible when the friction angle is higher than the slope angle, i.e.
307 in particular at flat or even counter slopes. We note that, by a simple transformation of Eq. 6, *FoM*
308 can alternatively be derived by relating the stopping time to the time step length. The stopping
309 criterion is only relevant for $v_0 > 0$.

310 *FoM* can relate to various spatial units: (i) a single cell, i.e. *FoM* is computed separately for each
311 cell. It may happen that stopping of the flow occurs at a certain cell, but not at its neighbour cells.
312 (ii) v_0 and β_v are averaged over a certain cell neighbourhood to compute *FoM*, so that stopping oc-
313 curs at patches of adjacent cells. (iii) β_v and the associated component of v are averaged over the
314 entire area of interest. This means that the entire flow stops at once.
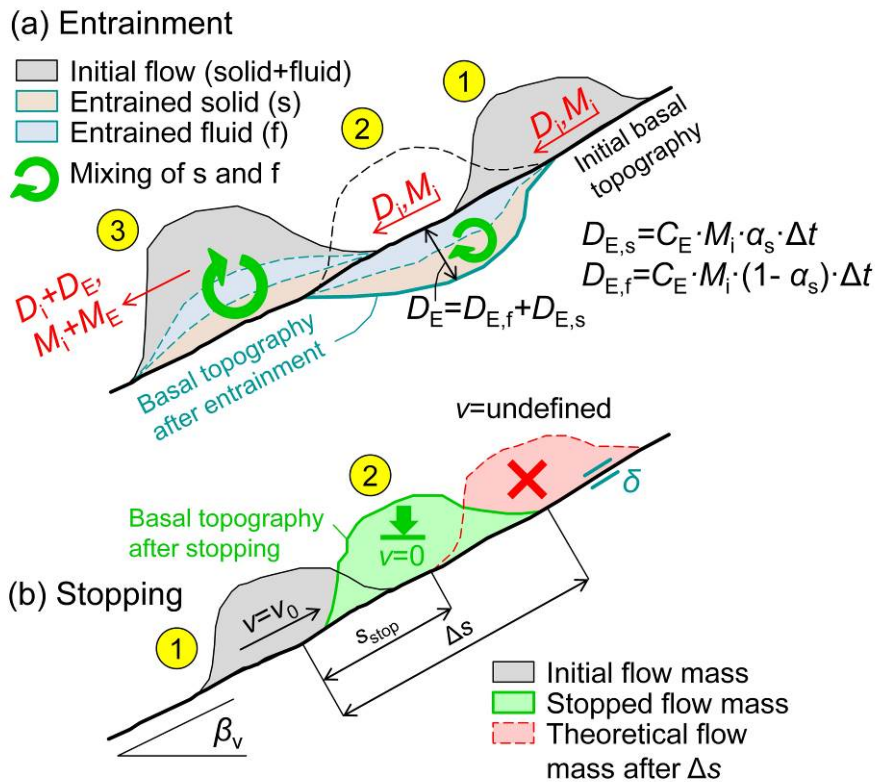
Figure 3 Interactions of the flow with the basal topography: (a) Entrainment, assuming that $H_{Emax,s}$ and $H_{Emax,f}$ are not limiting. D_i = total initial flow depth (s+f); M_i = total initial momentum (s+f); D_E = entrained depth; M_E = total increase in momentum due to entrainment (s+f). (b) Stopping and deposition. Both panels represent sections along the steepest slope of the basal topography. Note that stopping and deposition usually occur on less inclined slopes than drawn in (b) which represents upslope movement.

The third possibility is currently implemented with r.avaflow as an optional function. If activated, the simulation terminates as soon as stopping occurs and the entire flow material is deposited. Note that, in the current implementation, stopping and deposition always consider the total mass, without differentiating between the solid and the fluid components. This simplification is reasonable for flows characterized by a relatively small fluid volume fraction. The change of basal topography due to entrainment H_E after the last time step is subtracted from the height of the deposited material H_D in order to derive the change of basal topography (or net deposition) H_C at the end of the simulation (positive for an increase, negative for a decrease of terrain elevation).

2.5 Multiple model runs

r.avaflow includes a built-in function to perform multiple model runs at a time with controlled or random variation of uncertain input parameters between given lower and upper thresholds. Essentially, this concerns the flow parameters (see Table 2), but also the solid concentration of the release mass α_{s0}. Multiple parameters can be varied at a time. This procedure serves for two purposes:

- It facilitates multi-parameter sensitivity analysis and optimization efforts;

337   •   The results of all model runs are aggregated to an impact indicator index (III) and a deposi-
338   tion indicator index (DII), each in the range 0–1. III represents the fraction of model runs
339   where $H_{Max} \geq H_t$ at a given cell whilst DII represents the fraction of model runs where
340           $H_C \geq H_t$ at a given cell. III and DII are used to account for uncertain input parameters in
341   the simulation result.

342 The model runs can be split among multiple computational cores (parallel processing), enabling
343 the exploitation of high-performance computational environments (see Sect. 2.1).

2.6 Validation and visualization

345 r.avaflow can be used to produce map layouts and animations of the key results (see Fig. 1). It fur-
346 ther includes built-in functions to validate the model results against observations. Validation relies
347 (i) on the availability of a raster map of the observed impact or deposition area of the event under
348 investigation, (ii) on a user-defined profile along the main flow path (see Table 1), or (iii) on
349 measurements of H or v at selected coordinates and time steps. Those cells with observed impact
350 or deposition are referred to as observed positives (OP), those without observed impact or deposi-
351 tion as observed negatives (ON). When using the observed impact area (OIA) as reference, all cells
352 with $H_{Max} \geq H_t$ are considered as predicted positives (PP), all cells with $H_{Max} < H_t$ are considered as
353 predicted negatives (PN). When using the observed deposition area (ODA) as reference, all cells
354 with $H_C \geq H_t$ are considered as PP, all cells with $H_C < H_t$ are considered as PN. Intersecting ON and
355 OP with PP and PN results in four validation scores: true positive (TP), true negative (TN), false
356 positive (FP) and false negative (FN) predictions (Fig. 4). TN strongly depends on the size of the
357 area of interest. It is normalized to $5 \cdot (TP + FN) - FP$ in order to allow a meaningful comparison of
358 model performance among different case studies. These scores build the basis for most of the vali-
359 dation parameters described in Table 4. Only the excess travel distance ΔL relies on the observed
360 and simulated terminal points of the flow, based on a user-defined longitudinal profile. We note
361 that this profile is only needed for validation, but is not used for the mass flow simulation itself.

362 Values of $\Delta L > 0$ and $FoC > 1$ indicate conservative results (simulated impact or deposition area is
363 larger than observed impact or deposition area) whilst values of $\Delta L < 0$ and $FoC < 1$ indicate non-
364 conservative results. CSI, $D2PC$, and $AUROC$ do not allow to conclude on the conservativeness of
365 the results. ΔL, FoC, CSI, and $D2PC$ as defined in Table 4 target at the validation of H_{Max} or H_C de-
366 rived with one single model run. With multiple model runs (see Sect. 2.5) those validation param-
367 eters are computed separately for each run, allowing to conclude on the sensitivity of the model
368 performance to given input parameters, or to optimize input parameter values. In this sense, opti-
369 mum parameters always refer to one particular criterion, and different criteria may suggest differ-
370 ent optimum parameter values.

371 In contrast, ROC (Receiver Operating Characteristics) curves are used to test the performance of
372 the overall output of multiple model runs. Such curves are produced for III (OIA as reference)
373 and/or DII (ODA as reference): the true positive rate is plotted against the false positive rate for
374 various levels of III or DII. The area under the curve connecting the resulting points, $AUROC$, is

used as an indicator for model performance ($AUROC \approx 1$ indicates an excellent performance; see Fig. 4 and Table 4).

Further, the difference between observed and simulated values of H and v at selected sets of coordinates and points of time can be analyzed. This function is mainly useful for very well-documented case studies such as laboratory experiments and is not further used in the present work.
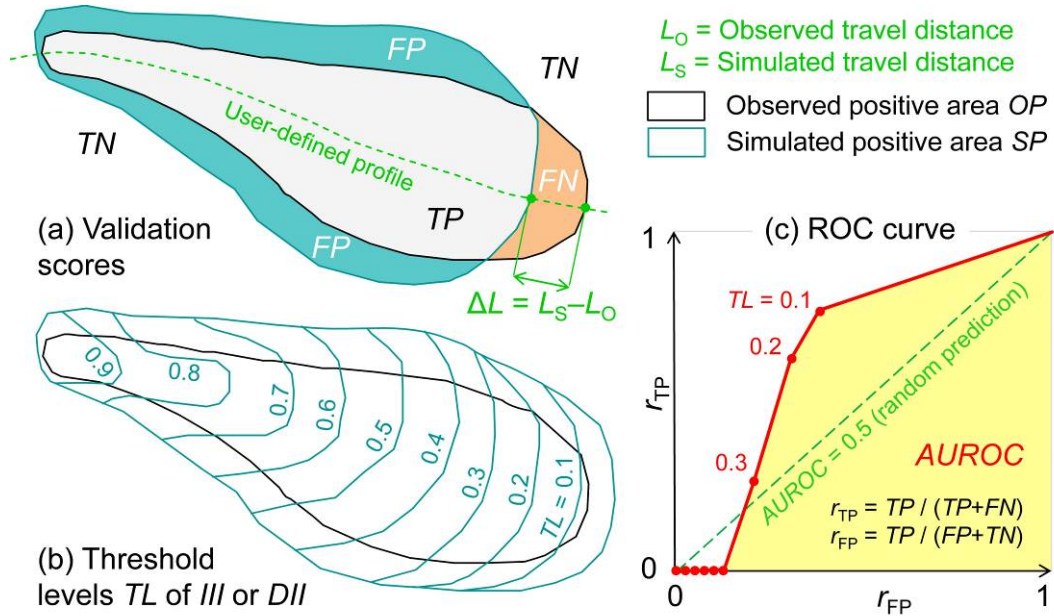
Figure 4 Validation of r.avaflow results. (a) Validation scores for single model run; (b) multiple model runs: threshold levels of III or DII, employed to produce (c) ROC curves.

Table 4 Validation criteria used in r.avaflow (see also Fig. 4). S = single model run, binary simulation result; M = multiple model runs, simulation result in the range 0–1. The concepts of CSI and $D2PC$ are taken from Formetta et al. (2015). All validation parameters are computed for H_{Max} (OIA as reference) and/or H_D (ODA as reference), depending on which of the reference data are available.

Scope	Name	Definition	Possible range	Optimum
S	Excess travel distance ΔL	$L_S - L_O$	$[-L_O, \infty]$	0.0
S	Factor of conservativeness FoC	$FoC = \dfrac{PP}{OP} = \dfrac{TP + FP}{TP + FN}$	$[0, \infty]$	1.0
S	Critical success index CSI	$CSI = \dfrac{TP}{TP + FP + FN}$	$[0,1]$	1.0
S	Distance to perfect classification $D2PC$	$D2PC = \sqrt{\left(1 - r_{TP}\right)^2 + r_{FP}^2}$ $r_{TP} = \dfrac{TP}{OP}, \; r_{FP} = \dfrac{FP}{ON}$	$[0,1]$	0.0
M	Area under ROC curve $AUROC$	Function of r_{TP} and r_{FP} for different levels of DII or III (see Fig. 4)	$[0.1]$	1.0
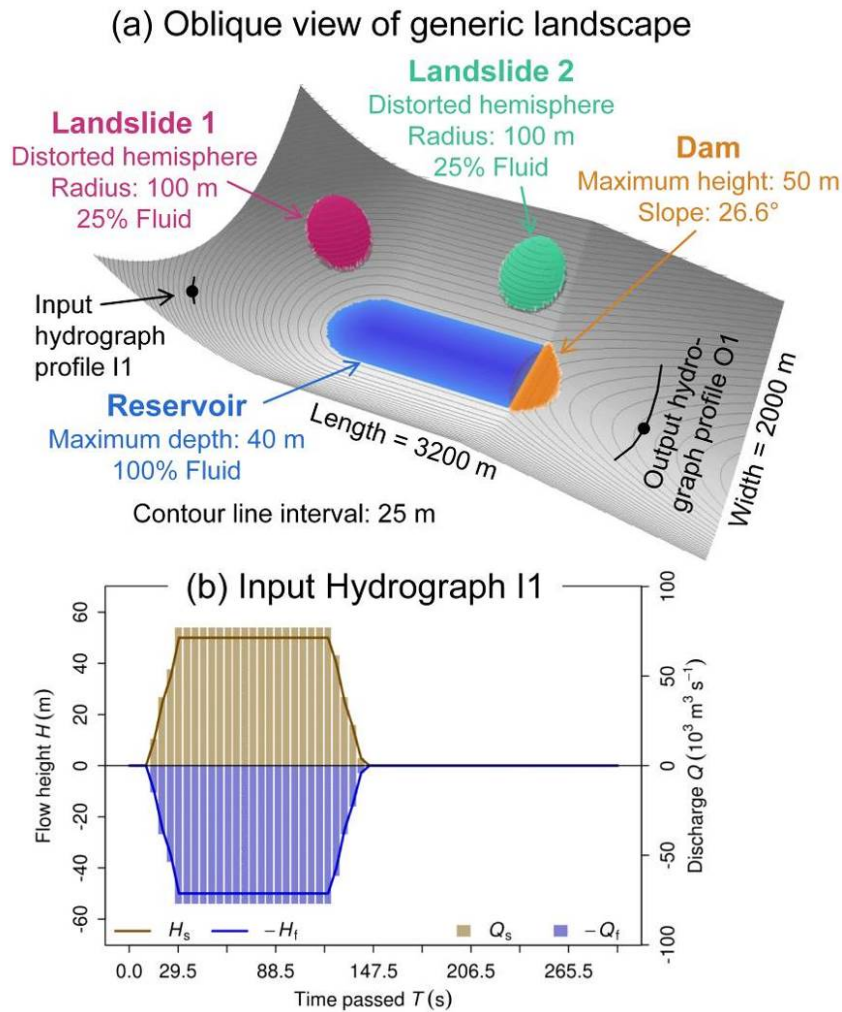
Figure 5 Generic landscape used for Experiment 1A–C. (a) Oblique view illustrating the topography and elements of the landscape. (b) Input hydrograph I1 employed for Experiment 1C.

3   Computational experiments

3.1   Experiment 1: Generic process chain

3.1.1   Topographic setup

In a first step, the potential of r.avaflow for simulating process chains is demonstrated, considering the interaction between one or more landslides, a reservoir, and the dam impounding the reservoir. This experiment represents a follow-up to the work of Pudasaini (2014); Kafle et al. (2016); and Kattel et al. (2016). We construct a generic landscape of size 3200 m · 2000 m, illustrated in Fig. 5a. This landscape consists of the following elements: (i) W–E stretching trough-shaped valley with an amphitheatre-shaped head, inclined towards E in its lower part; (ii) dam with a trapezoidal cross section running across the valley, consisting of 100% solid material; (iii) reservoir impounded by the dam; (iv) landslide release mass near the NW corner of the area of interest (Landslide 1); (v) landslide release mass directly N of the dam (Landslide 2); (vi) hydrograph release of landslide near the SW corner of the area of interest; (vii) measurement profile for output hydro-

406 graph downstream from the dam. Both landslide release masses assume the shape of a hemi-
407 ellipsoid imposed on the basal topography (see Fig. 5a). The algorithm for exactly reproducing the
408 generic landscape in GRASS GIS is available at http://www.avaflow.org/casestudies.html.

3.1.2 Modelling strategy and parameterization

410 The landslides 1 and 2 consist of 75% solid and 25% fluid by volume (uniformly mixed), the input
411 hydrograph I1 (see Fig. 5b) consists of 50% each solid and fluid per volume. The parameters and
412 settings applied are summarized in the Tables 2 and 3.

413 Three computational experiments are performed, with increasing complexity from A–C:

414 • Experiment 1A: Landslide 1 is released and interacts with the reservoir. The dam is as-
415 sumed stable and may therefore not be entrained.

416 • Experiment 1B: Again, Landslide 1 is released and interacts with the reservoir. However,
417 dam material is allowed to be entrained in this experiment.

418 • Experiment 1C: Landslide 2 is released and interacts with the dam and the reservoir. The
419 release from the input hydrograph I1 starts after 10 s and continues for a period of 130 s
420 (see Fig. 5). Dam material is allowed to be entrained at all stages of the computational ex-
421 periment.

422 All experiments are performed at a cell size of 10 m and for a duration of $t_{term} = 300$ s; $\Delta t_{out} = 5$ s.
423 The solid and fluid discharges are continuously recorded at the output hydrograph profile O1
424 downstream. The stopping function is deactivated (see Table 3).

3.1.3 Results

426 Animations illustrating the time evolution of the flow heights in all three experiments are en-
427 closed in Supp. 1A, 1B, and 1C.

428 Fig. 6a–f illustrates the flow heights at selected points of time during Experiment 1A. Landslide 1
429 (see Fig. 5a) impacts the backward portion of the reservoir after few seconds and generates a water
430 wave – oblique and perpendicular to the impact – that overtops the dam from $t = 50$–55 s onwards.
431 The output hydrograph O1 starts recording discharge at $t = 65$ s, with the peak of the first, major
432 flood wave passing at $t = 75$ s ($Q_f = 8 \cdot 10^4$ m^3 s^{-1}; Fig. 6g). We note that the discharge and the flow
433 height recorded by the hydrograph do not strictly follow the same pattern, as the discharge relates
434 to a profile and the flow height relates to a point (see Fig. 2). Meanwhile the impact wave is de-
435 flected at the dam and alleviates slowly. Further overtopping events caused by multiple deflections
436 of the alleviating wave occur mainly at the marginal parts of the dam at $t = 110, 150, 160, 200$ and
437 270 s, leading to smaller peaks in the output hydrograph ($Q_f = 1.5 \cdot 10^4$ m^3 s^{-1} at $t = 175$ s;
438 $Q_f = 2.2 \cdot 10^3$ m^3 s^{-1} at $t = 285$ s). The solid content passing the hydrograph profile is almost negligi-
439 ble as all solid landslide material remains in the reservoir basin. At $t = 300$ s, the impact wave in
440 the lake has almost alleviated (see Supp. 1A).

441 Experiment 1B (Fig. 7) is identical to the Experiment 1A until the point when the impact wave
442 reaches the dam at $t = 50$ s. Entrainment of the dam starts with overtopping which sets on at the

443   lateral portions. Part of the dam is entrained during overtopping by the initial impact wave.

444   Whilst massive outflow from the reservoir occurs due to the decreased level of the dam crest, part

445   of the wave is deflected at the dam and pushed back towards the rear part of the reservoir, induc-

446   ing a system of secondary waves. The remaining dam material is entrained when hit by those sec-

447   ondary waves. At $t = 200$ s the entire dam has disappeared and the reservoir starts emptying com-

448   pletely. In contrast to Experiment 1A, due to the emptying process, the system does not approach

449   a static equilibrium after $t = 300$ s (see Supp. 1B).

450   The temporal patterns of the simulated entrainment and wave propagation are clearly reflected in

451   the discharge recorded at the output hydrograph O1 (see Fig. 7g). As a consequence of dam over-

452   topping, fluid discharge at O1 starts increasing at $t = 65$ s and reaches a first peak at $t = 80$ s

453   ($Q_f = 5.1 \cdot 10^4$ m³). Solid discharge – a consequence of entrainment of the dam – starts slightly de-

454   layed, reaching a first peak roughly ten seconds later ($Q_s = 2.1 \cdot 10^4$ m³ s⁻¹). A depression in both of

455   the discharge curves at $t = 155$–160 s indicates that the initial impact wave has passed through. A

456   second, larger peak of fluid discharge is simulated at $t = 195$ s ($Q_f = 1.0 \cdot 10^5$ m³ s⁻¹). It occurs syn-

457   chronously with a second, smaller peak of solid discharge ($Q_s = 2.1 \cdot 10^4$ m³ s⁻¹), indicating a high

458   degree of mixing of the solid and fluid components of the flow. The pronounced second peak of Q_f

459   is a consequence of the secondary waves in combination with the lowered level of the dam. After

460   the peak, Q_s slowly and unsteadily decreases (the entire dam has been entrained and the material

461   has passed through) whilst Q_f remains high. Due to the entrainment of the dam, the simulated dis-

462   charges are much higher than those computed in the Experiment 1A (see Fig. 6g).

463   In Experiment 1C (Fig. 8) Landslide 2 impacts the dam and the frontal part of the reservoir less

464   than 10 s after release. The proximal portion of the dam is entrained rapidly. The E part of the

465   landslide moves outside of the reservoir in downstream direction. Consequently, the solid dis-

466   charge at the output hydrograph O1 starts at $t = 40$ s, reaching a peak of $Q_s = 2.4 \cdot 10^4$ m³ s⁻¹ five sec-

467   onds later (see Fig. 8g). Due to the high (75%) solid fraction of the landslide, the fluid discharge is

468   lower at that time ($Q_f = 1.5 \cdot 10^4$ m³ s⁻¹). The W part of the landslide interacts with the reservoir,

469   causing overtopping at the S (distal) portion of the dam. This results in the increase of fluid dis-

470   charge recorded at O1, culminating at $t = 60$ s when the solid discharge has already passed its peak

471   ($Q_f = 3.7 \cdot 10^4$ m³ s⁻¹). The resulting impact at O1 has reduced after $t = 105$ s in terms of discharge,

472   even though the total flow height remains at $H > 15$ m. This means that the flow material moves

473   slowly at O1.

474   From $t = 35$ s onwards the flow released through the input hydrograph I1 (see Fig. 5b) pushes the

475   reservoir water towards NE. The S part of the ramaining dam is overtopped by the resulting in-

476   homogeneous solid-fluid mixture (including material originating from Landslide 2), leading to

477   substantial further entrainment. In contrast to Experiment 1B, however, the dam is not complete-

478   ly entrained. The wave increasingly influences the discharge recorded at O1, leading to a peak at

479   $t = 180$ s ($Q_s = 6.9 \cdot 10^3$ m³ s⁻¹; $Q_f = 1.7 \cdot 10^4$ m³ s⁻¹). At that time the hydrograph indicates a well-

480   mixed flow with $\alpha_s \approx 0.25$, composed of fluid from the reservoir, solid-fluid mixtures from the

481   landslide and the hydrograph release, and solid material from the dam (see Fig. 5a). The solid and

fluid discharges remain at an almost constant level thereafter, reflecting a steady emptying of the reservoir.
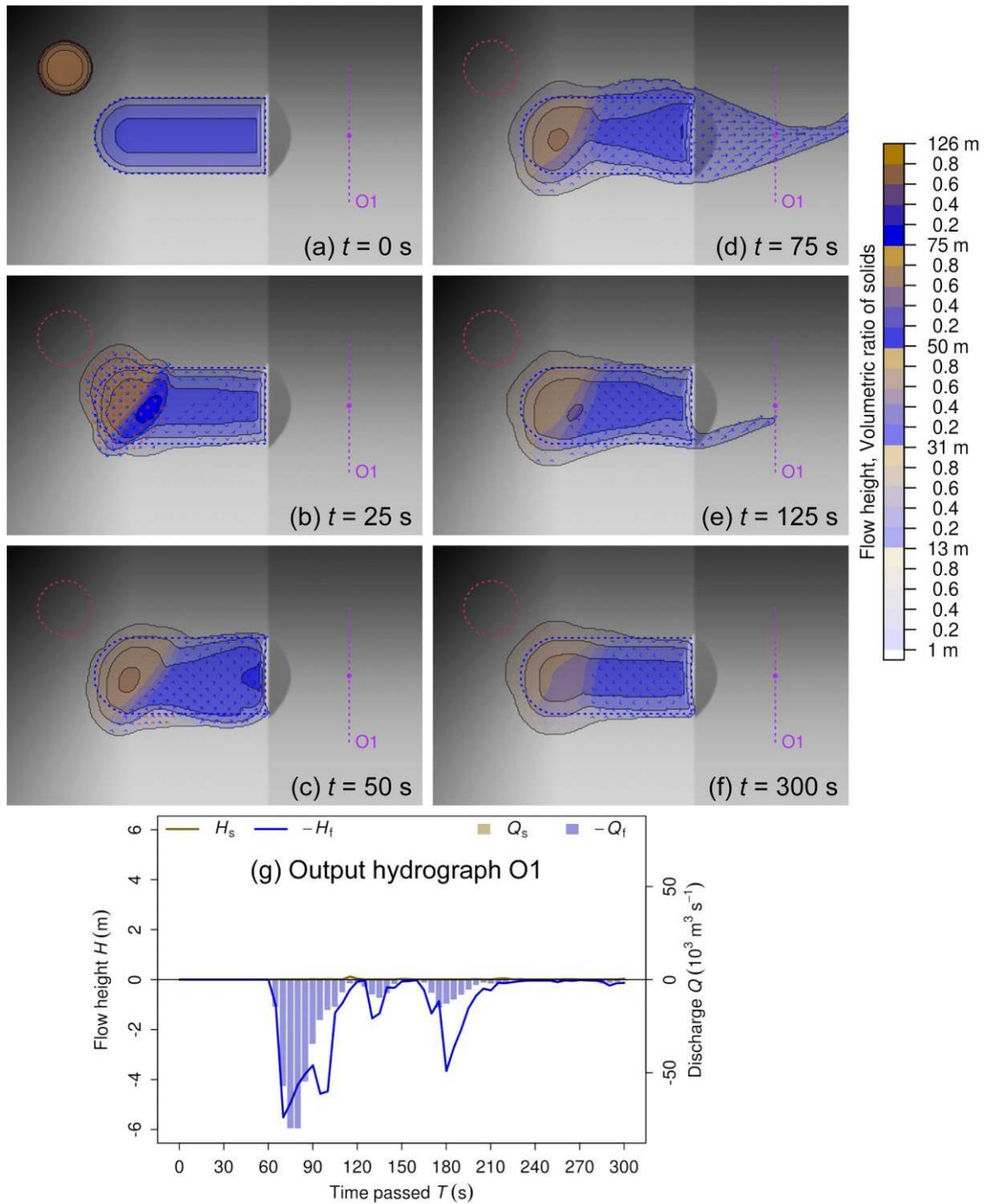
Figure 6 Key results of Experiment 1A. (a)–(f) Sequence of simulated flow heights and solid ratios at selected points of time; see Supp. 1A for animations of flow height and kinetic energy sequences; (g) output hydrograph O1 (see Fig. 5a).
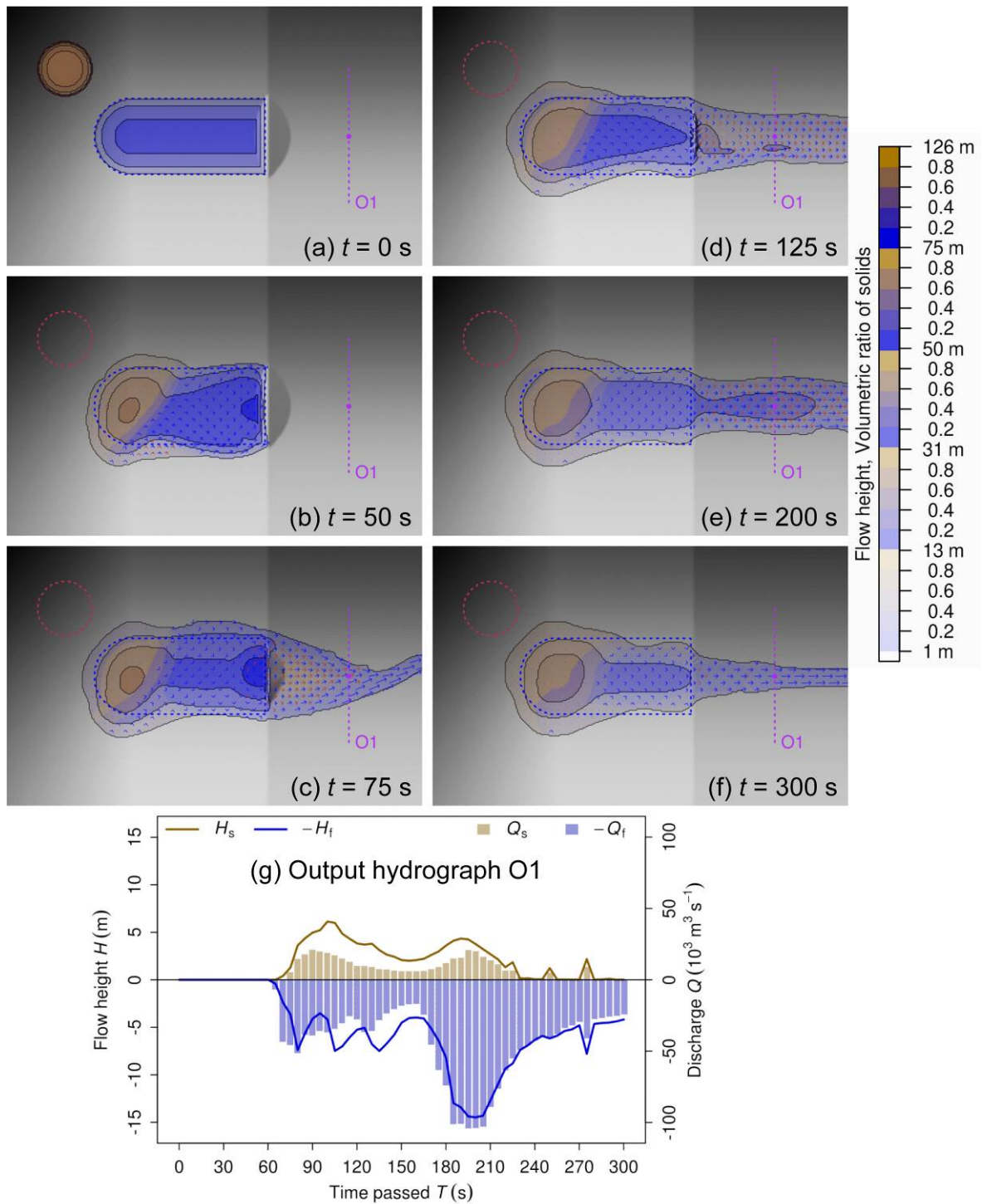
488
489   Figure 7 Key results of Experiment 1B. (a)–(f) Sequence of simulated flow heights and solid ratios
490   at selected points of time; see Supp. 1B for animations of flow height and kinetic energy sequenc-
491   es; (g) output hydrograph O1 (see Fig. 5a).
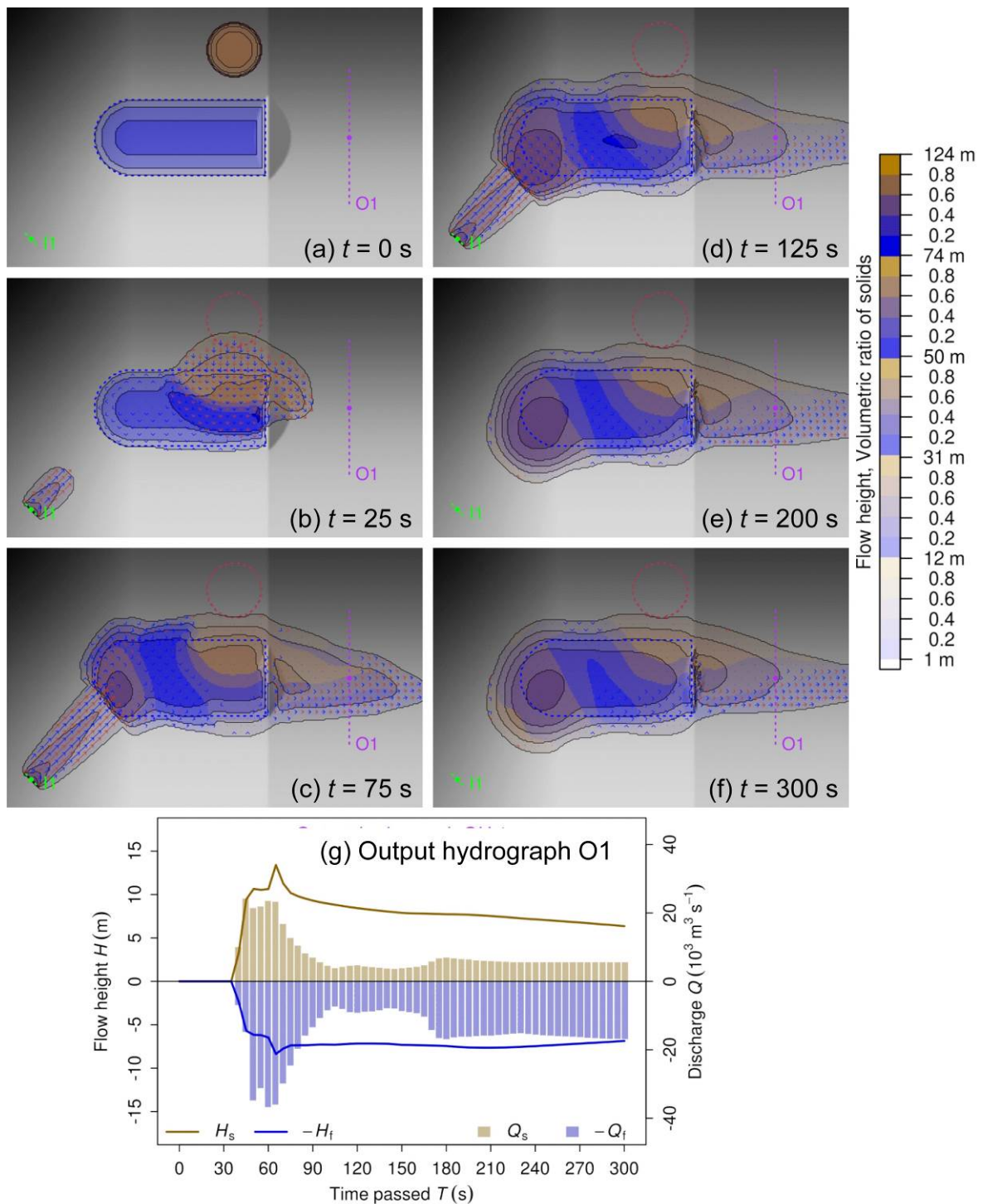
492
493 Figure 8 Key results of Experiment 1C. (a)–(f) Sequence of simulated flow heights and solid ratios
494 at selected points of time; see Supp. 1C for animations of flow height and kinetic energy sequenc-
495   es; (g) output hydrograph O1 (see Fig. 5a).

496

3.2 Experiment 2: Acheron rock avalanche, New Zealand

3.2.1 Event description

The Acheron rock avalanche in Canterbury, New Zealand (Fig. 9), occurred approx. 1,100 years BP (Smith et al., 2006). It is characterized by sharp bending of the flow path, a limited degree of spreading into the lateral valleys and a high mobility (travel distance: 3,550 m; measured angle of reach: 11.62°). It was used as a test event for the computational tool r.randomwalk (Mergili et al., 2015).

We employ a 10 m resolution DEM derived by stereo-matching of aerial photographs. ODA and OIA are derived from field and imagery interpretation as well as from data published by Smith et al. (2006). The OIA possibly underrepresents the real impact area as it might exclude some lateral and run-up areas of the rock avalanche not any more recognizable as such in the field. The distribution of release and deposition heights and an estimated release volume of $6.4 \cdot 10^6$ m³ are deduced from the reconstruction of the pre-event topography. According to this reconstruction, the maximum release height is 78.5 m whilst the maximum deposition height is 25.9 m.
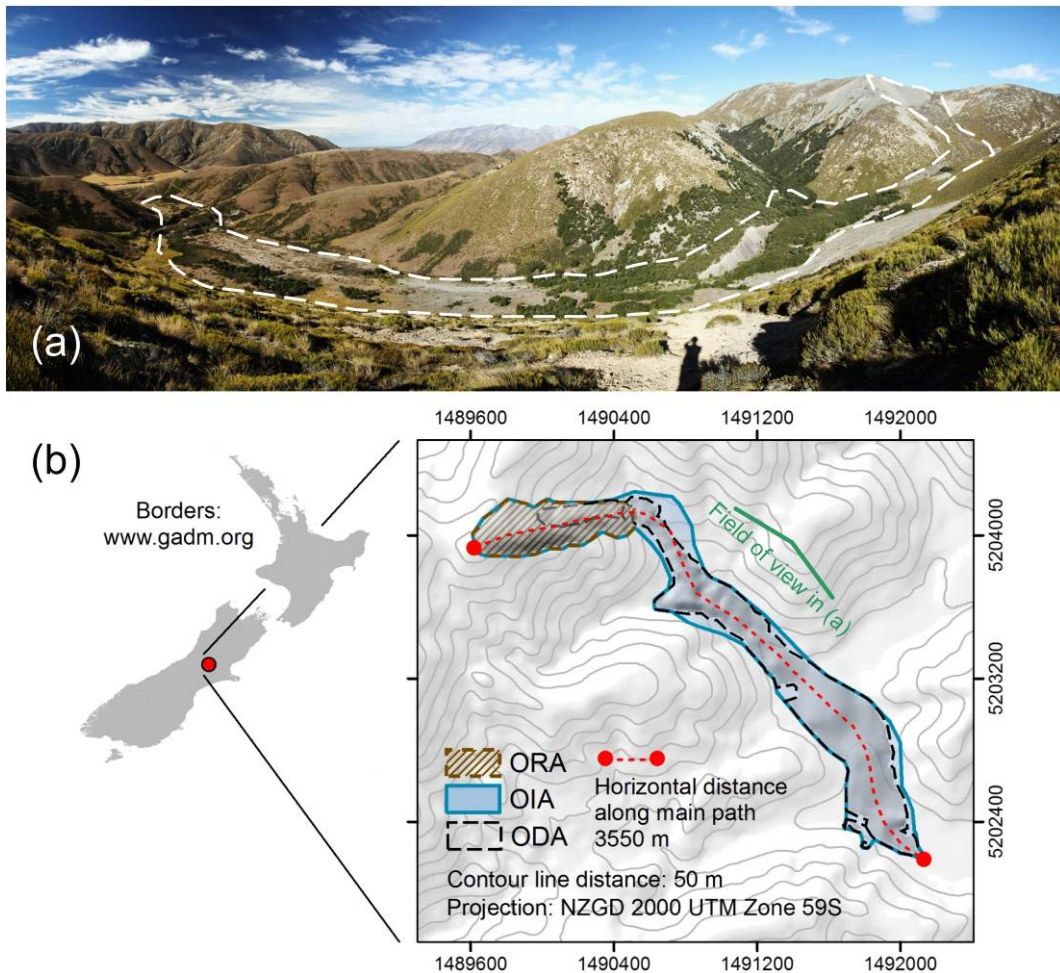
Figure 9 The Acheron rock avalanche. (a) Oblique view; the view point is indicated in (b) illustrating the location and the main elements of the rock avalanche; ORA = Observed release area.

3.2.2 Modelling strategy and parameterization

Preliminary tests have shown that the simulation results of r.avaflow are potentially sensitive to variations in the initial solid fraction α_{s0} and the basal friction angle δ, parameters which are uncertain in many real-world applications. We perform two computational experiments for the Acheron rock avalanche:

1. Experiment 2A: III and DII are computed from a set of 121 model runs. Thereby, α_{s0} is varied from 0.5–0.9, and δ is varied from 15–25° (see Table 2). The variation is done in a controlled way assuming a uniform probability density function, i.e. a regular grid with 11 grid points in each dimension is laid over the two-dimensional parameter space. III is then evaluated against the OIA, and DII is evaluated against the ODA. α_{s0} and δ are optimized in terms of ΔL, FoC, CSI, and $D2PC$ derived from H_D and the ODA.

2. Experiment 2B: r.avaflow simulation with the optimized values of α_{s0} and δ.

Both experiments are conducted at a cell size of 20 m. Entrainment is not considered whilst stopping and deposition are included (see Table 3). All flow parameters except for δ are kept constant (see Table 2).

3.2.3 Results

Fig. 10 illustrates III and DII derived with the parameter settings shown in the Tables 2 and 3 (Experiment 2A). $AUROC$ is 0.830 with regard to III and 0.838 with regard to DII. In general, those areas with high values of III coincide with the OIA, whilst those areas with lower values of III lie close to the margins or outside of the OIA. The performance of III suffers from the motion of small portions of the simulated avalanche in the wrong (N) direction and from excessive lateral spreading and run-up in the upper part, observed for all tested combinations of α_{s0} and δ (high values of III; see Fig. 10a). However, one has to consider that the event occurred hundreds of years ago and run-up may have occurred even though it is not any more recognizable in the field and therefore excluded from the OIA. High values of DII are fairly constrained to those cells within the ODA (see Fig. 10b) which is most probably better defined than the OIA. Those areas with lower, but non-zero values of III or DII both extend well beyond the reference areas. Particularly the travel distance appears highly sensitive to the choice of α_{s0} and δ.

We now focus on the DII map and evaluate the performance of the deposition maps simulated with the various combinations of α_{s0} and δ against the ODA. Fig. 11 illustrates the dependency of the model performance (defined by the parameters summarized in Table 4) on the combination of α_{s0} and δ employed for a given model run. All four parameters clearly indicate that, within the ranges tested, the model results are sensitive to both δ and α_{s0}. ΔL, CSI, and $D2PC$ display their optima near to $\delta = 17°$ as long as $\alpha_{s0} \geq 0.7$. With higher fluid content, the optimum value of δ increases, arriving at 20° with $\alpha_{s0} = 0.5$ (see Fig. 11a, b and d). This pattern appears plausible as far as a higher fluid content is supposed to increase the mobility of the flow, compensating for higher values of δ. However, values of $\alpha_{s0} < 0.7$ are not plausible at all for rock avalanches of this type. For $\alpha_{s0} \geq 0.7$ FoC displays its optimum of 1.0 at $\delta \geq 21°$, depending on α_{s0}. $FoC \approx 1.25$ for the value

552 of δ where the other parameters reach their optimum (see Fig. 11c). This would be fine for many
553 applications in practice where slightly conservative results are desirable.
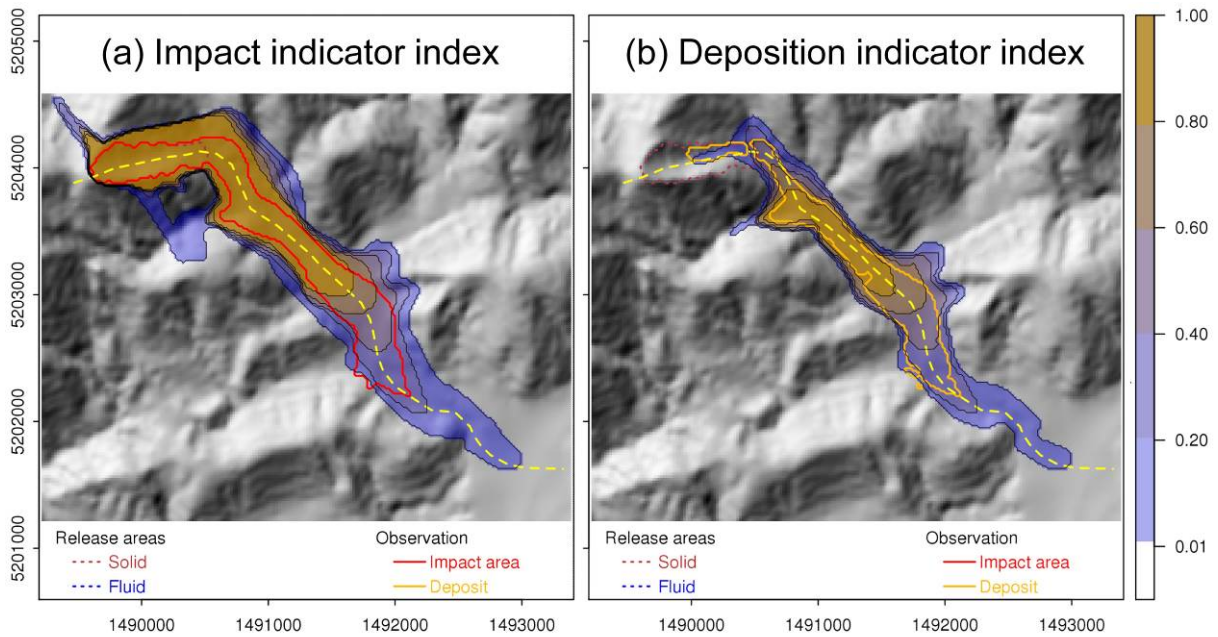
554
555 Figure 10 Results of Experiment 2A: (a) Impact indicator index III and (b) deposition indicator
556 index DII derived for the Acheron rock avalanche.

557
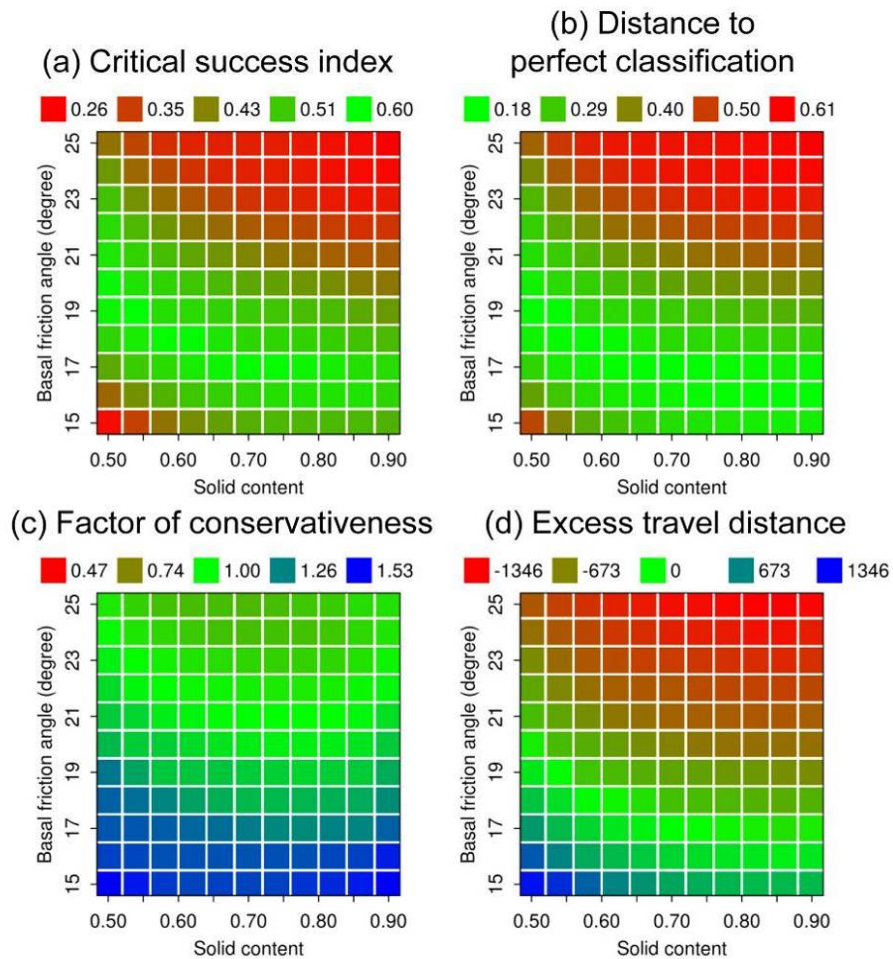
Figure 11 Validation and optimization of DII for the Acheron rock avalanche (see Table 4 for the criteria): (a) Critical success index CSI; (b) Distance to perfect classification $D2PC$; (c) Factor of conservativeness FoC; (d) Excess travel distance ΔL.

Consequently, we consider $\delta = 17°$ and $\alpha_{s0} = 0.8$ – in addition to the parameter values given in Table 2 – one possible combination for back-calculating the Acheron rock avalanche. The simulation is repeated with exactly this combination (Experiment 2B). We note, however, that these parameter values do not necessarily represent the real-world conditions as the fluid content of rock avalanches may be much lower. Fig. 12 shows the maps of H_{Max} and H_C, both corresponding reasonably well to the OIA and the ODA, respectively. The slightly larger simulated than observed deposit (see Fig. 12b) corresponds to $FoC \approx 1.25$, the almost perfect correspondence of the observed and simulated termini corresponds to $\Delta L \approx 0$. This means that the fact that the result is rather conservative than non-conservative ($FoC > 1$) relates to lateral spreading rather than to the travel distance of the rock avalanche. Supp. 2 illustrates the time evolution of the flow height in Experiment 2B.
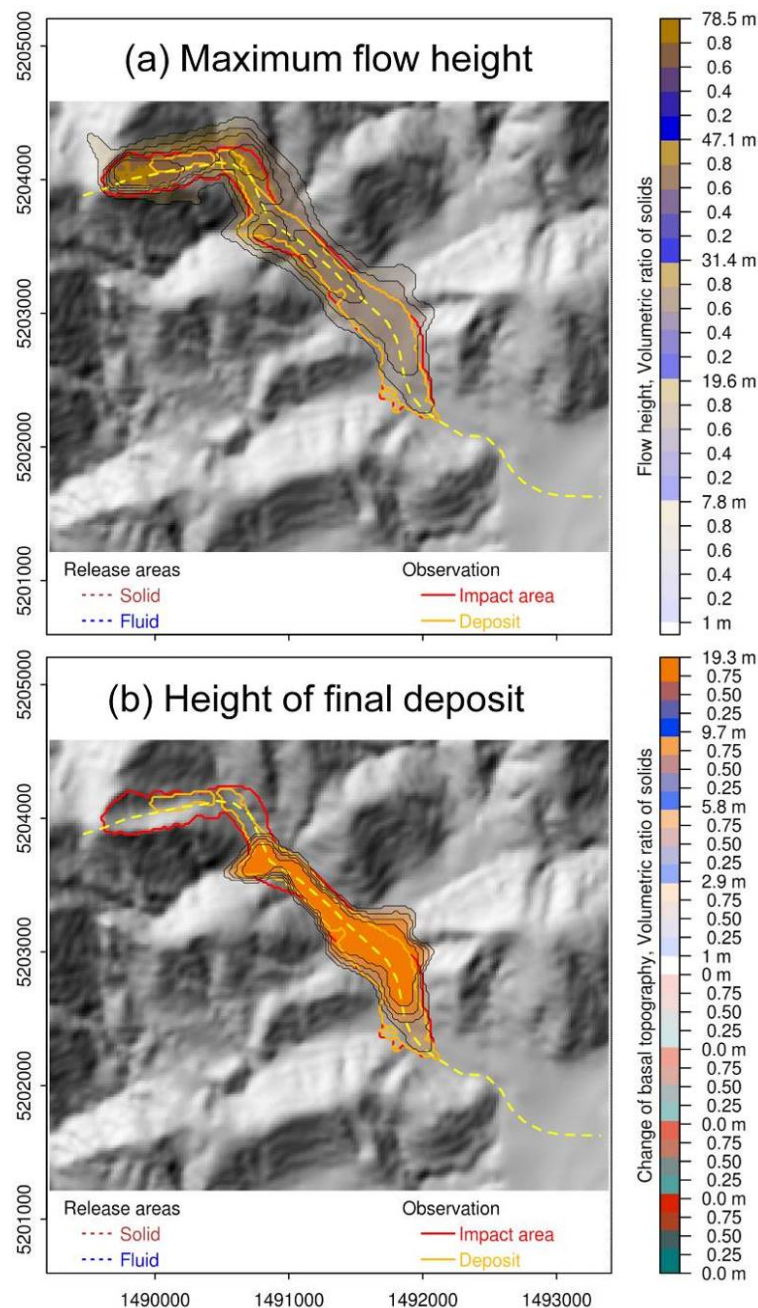
572
573 Figure 12 Results of Experiment 2B. (a) Maximum flow height H_{Max}; (b) Height of final deposit H_D
574 (as entrainment is not considered, $H_D = H_C$). Note that, due to the predominance of solids, the blu-
575 ish and greenish colours indicated in the legend do not appear in the map (see Figs. 6–8).

4   Discussion

577 The key purpose of the present article is to provide a general introduction to the key functionali-
578 ties of the computational tool r.avaflow. Thereby, the simulated patterns of flow height in Exper-
579 iment 1 (see Sect. 3.1) are plausible, and the agreement of the observed and simulated deposition
580 areas in Experiment 2B (see Sect. 3.2) appears reasonable. Yet, these experiments can neither re-
581 place model validation with observed process chains or interactions, nor thorough multi-
582 parameter sensitivity analysis and optimization efforts, which will both be the subjects of future
583 research. Fully documented two-phase process chains with readily available pre- and post-event

584 DTMs are scarce. Preliminary r.avaflow results for the 2012 Santa Cruz multi-lake outburst flood
585 in the Cordillera Blanca, Peru (Emmer et al., 2016) are, however, promising.

586 Experiment 2 serves for the demonstration of the parameter sensitivity analysis and optimization
587 functions of r.avaflow. The outcomes may be different when changing the cell size or any of the
588 flow parameter values (see Table 2). Making r.avaflow fit for forward predictions will require a
589 thorough multi-parameter sensitivity analysis and optimization campaign involving a large num-
590 ber and variety of well-documented events. Thereby we aim at obtaining guiding parameter val-
591 ues – or, more appropriately, guiding parameter ranges – for mass flow processes of different types
592 and magnitudes. Approaches to perform such analyses are readily available, and some of them can
593 be directly coupled to r.avaflow (Fischer, 2013; Fischer et al., 2015; Aaron et al., 2016; Krenn et al.,
594 2016). However, due to the complex nature of two-phase mixture flows, r.avaflow depends on a
595 relatively large number of flow parameters, a fact that represents a particular challenge in terms of
596 the computational resources as well as in terms of visualization and interpretation of the results of
597 multi-parameter studies.

598 r.avaflow represents a modular framework, allowing for the future enhancement of its particular
599 components. One issue concerns the numerical implementation of the two-phase model equa-
600 tions, combining topography-following coordinates with the quadratic cells of the raster data giv-
601 en in GIS coordinates (see Sect. 2.3). As in comparable simulation tools (e.g. Christen et al., 2010a,
602 b; Hergarten and Robl, 2015), approximations are currently used for coordinate transformation in
603 r.avaflow. This issue is closely related to the fact that the model equations that are commonly ex-
604 pressed in topography-following coordinates are hardly compatible with the data given in GIS co-
605 ordinates.

606 A detailed and fully discrete description of the TVD–NOC Scheme exists in the literature
607 (Wang et al., 2004), and the scheme served well for various theoretical test cases (e.g., Pudasaini
608 et al., 2014; Kafle et al.; 2016; Kattel et al., 2016). However, we also identify two major draw-
609 backs:

- 610 Although the numerical scheme itself should be shock capturing and volume preserving
  611 (Tai et al., 2002; Wang et al., 2004) these properties may not fully hold in practical appli-
  612 cations (i.e. bounded gravitational mass flows with well-defined margins over complex to-
  613 pography). The complementary functions with ID 1–3 introduced in Sect. 2.4 partly com-
  614 pensate for the issues raised.

- 615 For real flow applications, full handling of the evolution of the basal topography is not
  616 straightforward: the TVD-NOC scheme may introduce diffusion even though the evolu-
  617 tion of the basal topography is not a standard transport equation. Entrainment is therefore,
  618 as a first step, included as a complementary function.

619 The numerical scheme employed will have to be enhanced to directly and effectively incorporate
620 the complementary functions outlined in Sect. 2.4 in a fully consistent way. Extensions of similar
621 schemes have been tested for generic examples (e.g. Zhai et al., 2015) and could serve as a valuable
622 basis also to implement a mechanical model for erosion, entrainment and deposition (Pudasaini

and Fischer, 2016). On the one hand such an erosion model may build on existing concepts (e.g., Fraccarollo and Capart, 2002; Sovilla et al., 2006; Medina et al., 2008; Armanini et al., 2009; Crosta et al., 2009; Hungr and McDougall, 2009; Le and Pitman, 2009; Iverson, 2012; Pirulli and Pastor, 2012). On the other hand, it may further require some fundamentally new ideas with regard to deposition.

5 Conclusions and outlook

We have introduced r.avaflow, a multi-functional open source GIS application for simulating two-phase mass flows, process chains and interactions. The outcomes of two computational experiments have revealed that r.avaflow (i) has the capacity to simulate complex solid-fluid process interactions in a plausible way; and (ii) after the optimization of the basal friction angle and the solid content of the release mass, reasonably reproduces the observed deposition area of a documented rock avalanche. However, it was out of scope of the present work to validate the results obtained for complex process interactions against observed real-world data, or even to conduct a comprehensive multi-parameter optimization campaign. Such efforts will be the next step towards making r.avaflow ready for the forward prediction of possible future mass flow events. Thereby we will attempt to establish guiding parameter values for different types of processes and process magnitudes.

At the same time we have identified a certain potential for the future enhancement of some the components of r.avaflow. The key challenges will consist in (i) integrating the model equations in an up-to-date numerical scheme, allowing to directly include the complementary functions; and (ii) replacing the empirical entrainment model with a mechanical model for entrainment and deposition.

Code availability

The model codes, a user manual, the scripts used for starting the computational experiments presented in Sect. 3, and the GRASS locations with the spatial data necessary for reproducing the experiments are available at http://www.avaflow.org.

Acknowledgements

The work was conducted as part of the international cooperation project "A GIS simulation model for avalanche and debris flows (avaflow)" supported by the German Research Foundation (DFG, project number PU 386/3-1) and the Austrian Science Fund (FWF, project number I 1600-N30). We are grateful to Matthias Benedikt and Matthias Rauter for comprehensive technical support.

References

Aaron, J., Hungr, O., and McDougall, S.: Development of a systematic approach to calibrate equivalent fluid runout models. In: Aversa, S., Cascini, L., Picarelli, L., and Scavia, C. (eds): Landslides

657 and Engineered Slopes. Experience, Theory and Practice. Proc. 12th International Symposium of
658 Landslides, Napoli, Italy, 285–293, CRC Press, Boca Raton, London, New York, Leiden, 2016.

659 Armanini, A., Fraccarollo, L., and Rosatti, G.: Two-dimensional simulation of debris flows in erod-
660 ible channels. Comput. Geosci., 35, 993-1006, 2009.

661 Berger, C., McArdell, B. W., and Schlunegger, F.: Sediment transfer patterns at the Illgraben
662 catchment, Switzerland: Implications for the time scales of debris flow activities. Geomorphology,
663 125(3), 421–432, 2011.

664 Berger, M. J., George, D. L., LeVeque, R. J., and Mandli, K. T.: The GeoClaw software for depth-
665 averaged flows with adaptive refinement. Advan. Water Res., 34(9), 1195–1206, 2011.

666 Chen, H., Crosta, G. B., and Lee, C. F.: Erosional effects on runout of fast landslides, debris flows
667 and avalanches: A numerical investigation. Geotechnique, 56, 305–322, 2006.

668 Christen, C., Bartelt, P., and Kowalski, J.: Back calculation of the In den Arelen avalanche with
669 RAMMS: interpretation of model results. Ann. Glaciol., 51(54), 161–168, 2010a.

670 Christen, M., Kowalski, J., and Bartelt, B.: RAMMS: Numerical simulation of dense snow ava-
671 lanches in three-dimensional terrain. Cold Reg. Sci. Technol., 63, 1–14, 2010b.

672 Courant, R., Friedrichs, K., and Lewy, H.: On the partial difference equations of mathematical
673 physics. IBM J., 11(2), 215–234, 1967.

674 Crosta, G. B., Imposimato, S., and Roddeman, D.: Numerical modelling of entrainment/deposition
675 in rock and debris-avalanches. Eng. Geol., 109, 135–145, 2009.

676 Davis, S. F.: Simplified second-order Godunov-type methods. SIAM J. Sci. Stat. Comput., 9(3),
677 445–473, 1988.

678 Denlinger, R. P., and Iverson, R. M.: Granular avalanches across irregular three-dimensional ter-
679 rain: 1. Theory and computation. J. Geophys. Res., 109, F01014, 2004.

680 Emmer, A., Mergili, M., Juricová, A., Cochachin, A., and Huggel, C.: Insights from analyzing and
681 modelling cascading multi-lake outburst flood events in the Santa Cruz Valley (Cordillera Blanca,
682 Perú). Geophys. Res. Abstr., 18, 2181, 2016.

683 Evans, S. G., Bishop, N. F., Fidel Smoll, L., Valderrama Murillo, P., Delaney, K. B., and Oliver-
684 Smith, A: A re-examination of the mechanism and human impact of catastrophic mass flows origi-
685 nating on Nevado Huascarán, Cordillera Blanca, Peru in 1962 and 1970. Engin. Geol., 108, 96–118,
686 2009.

687 Fischer, J.-T.: A novel approach to evaluate and compare computational snow avalanche simula-
688 tion. Nat. Haz. Earth Syst. Sci., 13, 1655–1667, 2013.

689 Fischer, J. T., Kowalski, J., and Pudasaini, S. P.: Topographic curvature effects in applied avalanche
690 modeling. Cold Regions Sci. Technol., 74, 21–30, 2012.

691   Fischer, J.-T., Kofler, A., Fellin, W., Granig, M., and Kleemayr, K.: Multivariate parameter optimi-
692   zation for computational snow avalanche simulation in 3d terrain. J. Glaciol., 61(229), 875–888,
693   2015.

694   Formetta, G., Capparelli, G., and Versace, P.: Evaluating performances of simplified physically
695   based models for landslide susceptibility. Hydrol. Earth Syst. Sci. Discuss., 12, 13217–13256, 2015.

696   Fraccarollo, L., and Capart, H.: Riemann wave description of erosional dam-break flows. J. Fluid
697   Mech., 461, 183–228, 2002.

698   Gamma, P.: Dfwalk – Murgang-Simulationsmodell zur Gefahrenzonierung. Geographica Bernen-
699   sia, G66, 2000.

700   GRASS Development Team: Geographic Resources Analysis Support System (GRASS) Software,
701   Version 7.0. Open Source Geospatial Foundation, 2015. http://grass.osgeo.org, last access: 25 July
702   2016.

703   Grigoriyan, S. S., Eglit, M. E., and Yakimov, Y. L.: A new formulation and solution of the problem
704   of the motion of a snow avalanche. Trudy Vycokogornogo Geofiziceskogo Instituta, 12, 104–113,
705   1967.

706   Guzzetti, F.: Landslide hazard and risk assessment. PhD Dissertation, Bonn, 2006.

707   Hergarten, S., and Robl, J.: Modelling rapid mass movements using the shallow water equations in
708   Cartesian coordinates. Nat. Hazards Earth Syst. Sci., 15(3), 671–685, 2015.

709   Horton, P., Jaboyedoff, M., Rudaz, B., and Zimmermann, M.: Flow-R, a model for susceptibility
710   mapping of debris flows and other gravitational hazards at a regional scale. Nat. Haz. Earth Syst.
711   Sci., 13, 869–885, 2013.

712   Huggel, C., Zgraggen-Oswald, S., Haeberli, W., Kääb, A., Polkvoj, A., Galushkin, I., and Evans,
713   S.G.: The 2002 rock/ice avalanche at Kolka/Karmadon, Russian Caucasus: assessment of extraordi-
714   nary avalanche formation and mobility, and application of QuickBird satellite imagery. Nat. Haz.
715   Earth Syst. Sci., 5, 173–187, 2005.

716   Hungr, O., and McDougall, S.: Two numerical models for landslide dynamic analysis. Comput.
717   Geosci., 35(5), 978–992, 2009.

718   Hungr, O.: A model for the runout analysis of rapid flow slides, debris flows, and avalanches. Can.
719   Geotech. J., 32, 610–623, 1995.

720   Hungr, O., McDougall, S., and Bovis, M.: Entrainment of material by debris flows. In: Jakob, M.,
721   and Hungr, O. (eds.): Debris-flow hazards and related phenomena, 135–158, Springer, Berlin, Hei-
722   delberg, 2005b.

723   Hungr, O., and Evans, S. G.: Entrainment of debris in rock avalanches: an analysis of a long run-
724   out mechanism. Geol. Soc. Am. Bull., 116(9–10), 1240–1252, 2004.

725   Hungr, O., Corominas, J., and Eberhardt, E.: State of the Art paper: Estimating landslide motion
726   mechanism, travel distance and velocity. In: Hungr, O., Fell, R., Couture, R., Eberhardt, E. (eds.):

727 Landslide Risk Management. Proceedings of the International Conference on Landslide Management, Vancouver, Canada, 31 May – 3 June 2005, 129–158, 2005a.

729 Hutter, K., and Schneider L.: Important Aspects in the Formulation of Solid-Fluid Debris-Flow
730 models. Part I: Thermodynamic Implications. Continuum Mech. Thermodyn., 22(5), 363–390,
731 2010a.

732 Hutter, K., and Schneider L.: Important Aspects in the Formulation of Solid-Fluid Debris-Flow
733 models. Part II: Constitutive Modelling. Continuum Mech. Thermodyn., 22(5), 391–411, 2010b.

734 Iverson, R. M.: The physics of debris flows. Rev. Geophys., 35, 245–296, 1997.

735 Iverson, R. M.: Elementary theory of bed-sediment entrainment by debris flows and avalanches, J.
736 Geophys. Res., 117, F03006, 2012.

737 Iverson, R. M., and Denlinger, R. P.: Flow of variably fluidised granular masses across three-
738 dimensional terrain. I: Coulomb mixture theory. J. Geophys. Res., 106, 537–552, 2001.

739 Iverson, R. M., and George, D. L.: Modelling landslide liquefaction, mobility bifurcation and the
740 dynamics of the 2014 Oso disaster. Geotechnique, 66, 175–187, 2016.

741 Kafle, J., Pokhrel, P. R., Khattri, K. B., Kattel, P., Tuladhar, B. M., and Pudasaini, S. P.: Landslide-
742 generated tsunami and particle transport in mountain lakes and reservoirs. Ann. Glaciol, 57(71),
743 232–244, 2016.

744 Kattel, P., Khattri, K. B., Pokhrel, P. R., Kafle, J., Tuladhar, B. M., and Pudasaini, S. P.: Simulating
745 glacial lake outburst floods with a two-phase mass flow model. Ann. Glaciol., 57(71), 349–358,
746 2016.

747 Kowalski, J., and McElwaine, J. N.: Shallow two-component gravity-driven flows with vertical
748 variation J. Fluid Mech., 714, 434–462, 2013.

749 Krenn, J., Mergili, M., Fischer, J.-T., Frattini, P., and Pudasaini, S. P.: Optimizing the parameteri-
750 zation of mass flow models. In: Aversa, S., Cascini, L., Picarelli, L., and Scavia, C. (eds): Landslides
751 and Engineered Slopes. Experience, Theory and Practice. Proc. 12th International Symposium of
752 Landslides, Napoli, Italy, 1195–1203, CRC Press, Boca Raton, London, New York, Leiden, 2016.

753 Le, L., and Pitman, E. B.: A model for granular flows over an erodible surface. SIAM J. Appl.
754 Math., 70, 1407–1427, 2009.

755 Lied, K., and Bakkehøi, S.: Empirical calculations of snow-avalanche run-out distance based on
756 topographic parameters. J. Glaciol., 26, 165–177, 1980.

757 Mangeney, A., Bouchut, F., Lajeunesse, E., Aubertin, A., Vilotte, J. P., and Pirulli, M.: On the use
758 of Saint Venant equations to simulate the spreading of a granular mass. J. Geophys. Res., 110,
759 B09103, 2005.

760 Mangeney, A., Vilotte, J. P., Bristeau, M. O., Perthame, B., Bouchut, F., Simeoni, C., and Yerneni,
761 S.: Numerical modelling of avalanches based on Saint Venant equations using a kinetic scheme. J.
762 Geophys. Res., Solid Earth, 108, (B11)2527, 2003.

763 McDougall, S., and Hungr, O.: A Model for the Analysis of Rapid Landslide Motion across Three-
764 Dimensional Terrain. Canadian Geotech. J., 41, 1084–1097, 2004.

765 McDougall, S., and Hungr, O.: Dynamic modeling of entrainment in rapid landslides. Canadian
766 Geotech. J., 42, 1437–1448, 2005.

767 Medina, V., Hürlimann, M., and Bateman, A.: Application of FLATModel, a 2D finite volume
768 code, to debris flows in the northeastern part of the Iberian Peninsula. Landslides, 5, 127–142,
769 2008.

770 Mergili, M., Schratz, K., Ostermann, A., and Fellin, W.: Physically-based modelling of granular
771 flows with Open Source GIS. Nat. Haz. Earth Syst. Sci., 12, 187–200, 2012.

772 Mergili, M., Marchesini, I., Alvioli, M., Metz, M., Schneider-Muntau, B., Rossi, M., and Guzzetti,
773 F.: A strategy for GIS-based 3D slope stability modelling over large areas. Geosci. Model Dev., 7,
774 2969–2982, 2014.

775 Mergili, M., Krenn, J., and Chu, H.-J.: r.randomwalk v1, a multi-functional conceptual tool for
776 mass movement routing. Geosci. Model Dev. 8, 4027–4043, 2015.

777 Nessyahu, H., and Tadmor, E.: Non-oscillatory central differencing for hyperbolic conservation
778 laws. J. Comput. Phys., 87, 408–463, 1990.

779 Neteler, M., and Mitasova, H.: Open source GIS: a GRASS GIS approach. Springer, New York,
780 2007.

781 Pastor, M., Haddard, B., Sorbino, G., Cuomo, S., and Drempetic, V.: A depth-integrated, coupled
782 SPH model for flow-like landslides and related phenomena. Int. J. Num. Anal. Meth. Geomech.,
783 33, 143–172, 2009.

784 Pirulli, M., and Pastor, M.: Numerical study on the entrainment of bed material into rapid land-
785 slides. Geotechnique, 62, 959–972, 2012.

786 Pitman, E. B., and Le, L.: A two-fluid model for avalanche and debris flows. Phil. Trans. R. Soc.
787 A363, 1573–1601, 2005.

788 Pitman, E. B., Nichita, C. C, Patra, A. K, Bauer, A. C., Bursik, M., and Weber, A.: A model of gran-
789 ular flows over an erodible surface. Discrete Contin. Dynam. Syst. B., 3, 589–599, 2003a.

790 Pitman, E. B., Nichita, C. C., Patra, A. K., Bauer, A., Sheridan, M., and Bursik, M.: Computing
791 granular avalanches and landslides. Phys. Fluids, 15(12), 3638–3646, 2003b.

792 Popinet, S.: An accurate adaptive solver for surface-tension-driven interfacial flows, J. Comput.
793 Phys., 228, 5838–5866, 2009.

794 Pudasaini, S. P.: A general two-phase debris flow model, J. Geophys. Res., 117, F03010, 2012.

795 Pudasaini, S. P.: Dynamics of submarine debris flow and tsunami. Acta Mech., 225, 2423,
796 doi:10.1007/s00707-014-1126-0, 2014.

797 Pudasaini, S. P., and Fischer, J.-T.: A mechanical erosion model for two-phase mass flows.
798 arXiv:1610.01806, 2016.

799 Pudasaini, S. P., and Hutter, K.: Rapid shear flows of dry granular masses down curved and twisted
800 channels. J. Fluid Mech., 495, 193–208, 2003.

801 Pudasaini, S. P., and Hutter, K.: Avalanche Dynamics: Dynamics of rapid flows of dense granular
802 avalanches. Springer, Berlin, Heidelberg, 2007.

803 Pudasaini, S. P., and Krautblatter, M.: A two-phase mechanical model for rock-ice avalanches. J.
804 Geophys. R.: Earth Surf., 119(10), 2272–2290, 2014.

805 Pudasaini, S. P., Wang, Y., and Hutter, K.: Modelling debris flows down general channels. Nat.
806 Hazards Earth Syst. Sci., 5(6), 799–819, 2005.

807 Pudasaini, S. P., Wang, Y., Sheng, L.-T., Hsiau, S.-S., Hutter, K., and Katzenbach, R.: Avalanching
808 granular flows down curved and twisted channels: Theoretical and experimental results. Phys.
809 Fluids, 20, 073302, 2008.

810 R Core Team: R: A Language and Environment for Statistical Computing. R Foundation for Statis-
811 tical Computing, Vienna, Austria, http://www.R-project.org, last access: 25 July 2016.

812 Reid, M. E., Iverson, R. M. , Logan, M. , Lahusen, R.G., Godt, J.W., and Griswold, J.P.: Entrain-
813 ment of bed sediment by debris flows: results from large-scale experiments. In: Genevois, R.,
814 Hamilton, D. L., and Prestininzi, A. (eds.): Proc. 5th International Conference on Debris-Flow
815 Hazards Mitigation: Mechanics, Prediction and Assessment, Padua, Italy (Italian Journal of Engi-
816 neering Geology and Environment – Book), 367-374, La Sapienza, Rome, 2011.

817 Rickenmann, D., Weber, D., and Stepanov, B.: Erosion by debris flows in field and laboratory ex-
818 periments. In: Rickenmann, D., and and Chen, C.-L. (eds.): Proc. 3rd International Conference on
819 Debris-Flow Hazards Mitigation: Mechanics, Prediction, and Assessment, Davos, Switzerland,
820 883–894. Millpress, Rotterdam, 2003.

821 Sampl, P., and Zwinger, T.: Avalanche Simulation with SAMOS. Ann. Glaciol., 38, 393–398, 2004.

822 Savage, S. B., and Hutter, K.: The motion of a finite mass of granular material down a rough in-
823 cline. J. Fluid Mech., 199, 177–215, 1989.

824 Savage, S. B., and Iverson, R. M.: Surge dynamics coupled to pore-pressure evolution in debris
825 flows. In: Rickenmann, D., and Chen, C.-L. (eds): Proc. 3rd International Conference on Debris-
826 Flow Hazards Mitigation: Mechanics, Prediction and Assessment, Davos, Switzerland, 503–514.
827 Millpress, Rotterdam, 2003.

828 Smith, G. M., Davies, T. R., McSaveney, M. J., and Bell, D. H.: The Acheron rock avalanche, Can-
829 terbury, New Zealand – morphology and dynamics. Landslides, 3, 62-72, 2006.

830 Sovilla, B., Burlando, P., and Bartelt, P.: Field experiments and numerical modeling of mass en-
831 trainment in snow avalanches. J. Geophys. Res., 111, F03007, 2006.

832 Tai, Y. C., Noelle, S., Gray, J. M. N. T., and Hutter, K.: Shock-capturing and front-tracking meth-
833 ods for granular avalanches. J. Comput. Phys., 175, 269–301, 2002.

834 Takahashi, T.: Debris Flow. IAHR Monograph Series, Balkema, The Netherlands, 1991.

835 Toro, E. F.: Riemann problems and the waf method for solving the twodimensional shallow water
836 equations. Philos. Trans. R. Soc. London A, 338, 43–68, 1992.

837 Van Westen, C. J., van Asch, T. W. J., and Soeters, R.: Landslide hazard and risk zonation : why is
838 it still so difficult? Bull. Eng. Geol. Environ, 65(2), 176–184, 2005.

839 Voellmy, A.: Über die Zerstörungskraft von Lawinen. Schweizerische Bauzeitung 73, 159–162,
840 212–217, 246–249, 280–285, 1955.

841 Wang, Y., Hutter, K., and Pudasaini, S. P.: The Savage-Hutter theory: A system of partial differen-
842 tial equations for avalanche flows of snow, debris, and mud. J. Appl. Math. Mech., 84, 507–527,
843 2004.

844 Wichmann, V., and Becht, M.: Modelling of Geomorphic Processes in an Alpine Catchment. In:
845 Proceedings of the 7th International Conference on GeoComputation, Southampton. 14 pp., 2003.

846 Zhai, Q., Zhang, R., and Wang, X.: A hybridized weak Galerkin finite element scheme for the
847 Stokes equations. Sci. China Math., 58(11), 2455–2472, 2015.